An atlas of microtubule lattice parameters regulated through ligand binding to the microtubule stabilizing sites.

Lucena-Agell, D.[1*]; Fernández, Ó.[1*]; París-Ogáyar, R.[1,2*]; Estévez-Gallego, J.[3], Ondruskova, D.[4]; Álvarez-Bernad, B. [1]; Bonato, F. [1]; Larraga, J. [1], Ortiz de Elguea, D. [1]; Cano, G.J. [1]; Scheers, M. [1]; Imai, H. [5]; Yagi, T. [6]; Iwamoto, H.[7]; Martínez-Guil, J. C. [8]; Singh, A.J.[9]; Keyzers, R.A.[10], Vanderwal, C. [11], Altmann, K.-H. [12]; Van der Eycken, J. [13]; Palomo, V.[2]; Fang, W-S.[14]; Gago, F. [15]; Lansky, Z.[4]; Braun, M.[4]; Oliva, M.A.[1]; Kamimura, S.[16]; Díaz, J.F.[1]

[1]Unidad BICS, Centro de Investigaciones Biológicas Margarita Salas, Consejo Superior de Investigaciones Científicas, 28040 Madrid, Spain.

[2]Instituto Madrileño de Estudios Avanzados en Nanociencia (IMDEA-Nanociencia), Madrid, Spain.

[3]Laboratory of Biomolecular Research, Department of Biology and Chemistry, Paul Scherrer Institute, Villigen, Switzerland.

[4]Institute of Biotechnology of the Czech Academy of Sciences, BIOCEV, Prague West, Czech Republic.

[5]Department of Biological Sciences, Graduate School of Science, Osaka University, Japan.

[6]Department of Life Sciences, Faculty of Biological Resources, Prefectural University of Hiroshima, Japan.

[7]Research & Utilization Division, Japan Synchrotron Radiation Research Institute (JASRI), SPring-8, Japan.

[8]ALBA Synchrotron, CELLS, Cerdanyola del Vallès 08290, Spain.

[9]Ferrier Research Institute, and Centre for Biodiscovery, Victoria University of Wellington, PO Box 600, Lower Hutt 5010, New Zealand.

[10]School of Chemical & Physical Sciences, and Centre for Biodiscovery, Victoria University of Wellington, PO Box 600, Wellington 6140, New Zealand.

[11]Department of Chemistry, 1102 Natural Sciences II, and Department of Pharmaceutical Sciences, 856 Health Sciences Road, Suite 5400, University of California, Irvine, CA 92697, USA.

[12]ETH Zurich, Department of Chemistry and Applied Biosciences, Institute of Pharmaceutical Sciences, 8093 Zürich, Switzerland.

[13]Department of Organic and Macromolecular Chemistry, Faculty of Sciences, Ghent University, Krijgslaan 291 (S.4), B-9000 GHENT, Belgium.

[14]Institute of Materia Medica, Chinese Academy of Medical Sciences & Peking Union Medical College, 2A Nan Wei Road, Beijing 100050.

[15]Department of Biomedical Sciences, University of Alcalá, Madrid, Spain.

[16]Department of Biological Sciences, Faculty of Science and Engineering, Chuo University, Tokyo, Japan.

*These authors have contributed equally.

ABSTRACT

Microtubules (MTs) are essential cytoskeletal polymers with dual functions: they generate mechanical forces necessary for processes such as mitosis and angiogenesis, and serve as static tracks for intracellular transport by motor proteins. Force generation is mediated by the cytomotive switch, a dynamic property modulated by MT stability. Second-generation microtubule-targeting agents (MTAs), such as paclitaxel and docetaxel, bind at the taxane site and chemically stabilize MTs by enhancing lateral and longitudinal tubulin interactions. While effective in blocking MT depolymerization and preserving transport, the fact that these drugs introduce structural alterations that distinguish stabilized MTs from their native counterparts raises concerns for both mechanistic studies and clinical applications in diseases like tauopathies.

In this study, we provide a detailed structural atlas of taxane site-mediated modulation of MTs. We show that drug binding induces two distinct lattice conformations in the longitudinal axis—expanded (4.17 nm rise) and compressed (4.06 nm rise)—with rapid transitions and low energy barriers between them. In contrast, lateral interactions allow multiple protofilament (PF) configurations with small energetic differences but high activation barriers, a finding consistent with the observed structural heterogeneity of MTs. Notably, minor chemical modifications, such as acetylation of paclitaxel's C-7 hydroxyl, can shift these conformational equilibria. These structural changes significantly impact biochemical properties, and alter recognition by tau and kinesin proteins, suggesting a role for lattice conformation as a signaling cue. Our findings underscore the nuanced structural consequences of taxane-site ligand binding and its relevance in both therapeutic and experimental contexts.

Introduction

Microtubules (MTs) are cellular structures involved in many essential biological processes. They are polymers composed of tubulin, a heterodimer of α- and β-tubulin, which serves as their main structural component. Microtubules are responsible for generating cellular forces, maintaining cell shape, and providing polarized tracks for directional, motor-mediated chemical transport (1).

Tubulin, together with actin, generates mechanical forces by coupling nucleotide hydrolysis to its polymerization cycle. Both proteins undergo assembly state-dependent conformational changes that are intrinsically linked to their ability to produce force—a mechanism known as the cytomotive switch (2). In tubulin, this switch entails a curved-to-straight conformational transition characterized by an interdomain rotation between the N- and C-terminal domains of each monomer, accompanied by a downward displacement of helix H7 (3-5).

Because this conformational change is essential for force generation, compounds that block the transition inhibit cellular processes that depend on mechanical force—such as cell division and angiogenesis—thereby severely compromising cell function. Consequently, many sessile organisms have evolved to produce tubulin-targeting anticytomotive compounds as a defense mechanism against predators (6). These compounds bind to the αβ-tubulin heterodimer on at least eight distinct binding sites (7-9), employing four main mechanisms to block the cytomotive switch.

Compounds that inhibit MT formation act on six distinct binding sites—those of colchicine, vinblastine, maytansine, pironetin, gatorbulin, and todalam. These compounds block the cytomotive switch through two main mechanisms:

(i) some compounds bind at the intradimer interface, acting as molecular wedges that trap tubulin in the assembly-incompetent curved conformation. Representative examples include colchicine, derived from *Colchicum autumnale*, the extract from which as a gout treatment has been documented since 1500 BC (10); mebendazole, a well-established anthelmintic (11); and gatorbulin, a recently discovered tubulin inhibitor that binds to a novel site(8).

(ii) other compounds that block longitudinal interdimer interfaces, such as vinblastine, the first tubulin-targeting agent approved for cancer therapy (12); maytansine, one of the most widely used payloads in antibody-drug conjugates (ADCs) (13), and pironetin (14). By binding at these longitudinal contacts, these ligands prevent the addition of new subunits and subsequently the conformational transition (15-18). As a result, ligand-bound subunits become inactive, leading to the collapse of the microtubule network and inhibition of cell division in rapidly proliferating cells, such as leukemic cells.

Although first-generation tubulin inhibitors (e.g., vinca alkaloids) are highly effective against rapidly dividing tumors—by blocking the force generation required for cell division and migration—their mechanism of action involves the destruction of microtubules. These compounds inhibit the cytomotive switch in the curved-to-straight direction, thereby preventing polymerization. Consequently, they indiscriminately block all tubulin-mediated functions, not only those related to force generation but also structural roles essential for intracellular transport, axonal integrity, and

neural transmission. This broad inhibition leads to one of the most limiting side effects in successful cancer therapy: peripheral neurotoxicity, caused by damage or degeneration of peripheral nerves (19).

Paclitaxel (Taxol®) was the first representative of the second generation of microtubule-targeting agents (MTAs), approved for clinical use in 1992 (20). This second family, later expanded to include docetaxel (Taxotere®), cabazitaxel (Jevtana®), and ixabepilone (Ixempra®), acts through the opposite mechanism to that of the vinca alkaloids—blocking the cytomotive switch in the straight-to-curved direction. The resulting stabilization of microtubules defines these compounds as microtubule-stabilizing agents (MSAs).

Structural studies of MSA–tubulin interactions have revealed two distinct mechanisms, involving two different binding sites, that prevent the straight-to-curved transition. Most known MSAs—including taxanes, epothilones, discodermolides, and zampanolides—bind to the taxane site, where they reinforce lateral contacts between tubulin subunits by pushing the S9–S10 loop (M-loop) toward the interprotofilament (IPF) space (21). In contrast, compounds that bind to the laulimalide/peloruside site (22) stabilize MTs by bridging adjacent PFs, thereby also preventing the straight-to-curved transition. Although this mechanism should, in principle, selectively target MT force-generating functions while preserving their structural and trafficking roles, MSAs exhibit peripheral neurotoxic effects that are comparable to—or even more severe than—those caused by microtubule-destabilizing agents (MDAs) (23, 24).

Structural studies on the most commonly used second-generation microtubule-targeting drugs indicate that their stabilizing effect on microtubules is not without structural consequences. Binding of paclitaxel and docetaxel to the taxane site induces a longitudinal expansion of the microtubule lattice, increasing the dimer repeat distance from 4.06 nm to 4.17 nm; in the case of paclitaxel, this also enlarges the IPF angle, resulting in thinner MTs (21). In contrast, compounds that bind to the laulimalide/peloruside site stabilize MTs without lattice expansion, although they cause distortions at the lateral interface. Nevertheless, it is possible to design compounds targeting this site—such as pelophen B—that stabilize MTs without introducing structural distortions (25).

MT structure plays a central role in its own regulation, which occurs at several levels, the first being the nucleotide bound to the exchangeable site. Tubulin bound to GTP incorporates into the growing plus end of the MT. Because the nucleotide binding site lacks a catalytic residue required for hydrolysis—supplied instead by the next incoming tubulin subunit—activation of GTPase activity occurs stochastically. As a result, a chemical gradient is established along the MT, from GTP-bound tubulin at the plus end to GDP-bound tubulin within the lattice core. In this way, the nucleotide-driven chemical gradient is translated into subtle structural variations within the MT lattice that are recognized by microtubule-associated proteins (MAPs) (1, 26). MAPs represent the principal endogenous regulators of MT dynamics and orchestrate the structural remodeling of MT networks, which is essential for optimal cellular functionality (27). Several examples illustrate this structural recognition. End-binding (EB) proteins display selective affinity for the GTP-rich plus ends of microtubules (28), while tau and kinesin exhibit preferential binding

142 to lattices with specific monomer-to-monomer spacings. Kinesin-1, for instance, shows enhanced
143 affinity in gliding assays for MTs with an expanded lattice (4.17 nm spacing) (29), whereas tau
144 preferentially associates with compacted lattices (4.06 nm spacing).
145 Moreover, *in vitro* evidence demonstrates that tau cooperatively induces lattice
146 compaction in microtubules that have been exogenously expanded by paclitaxel (30), whereas
147 kinesin has been shown to promote lattice expansion (31). These differential preferences likely
148 reflect the dual functional capacity of these proteins to both recognize specific conformational
149 states and actively remodel the microtubule lattice. Collectively, the literature suggests that tau
150 and kinesin act as both sensors and effectors of the MT lattice. Consequently, compounds that
151 induce structural distortions in MTs are expected to strongly influence MAP recognition and
152 activity, thereby disrupting the regulation of MT dynamics and function (32).
153 Given the central role of tubulin-targeted therapies and their potential to address
154 inflammatory, neoplastic, and neurodegenerative diseases, it is of utmost importance to
155 understand how MSAs alter MT structure. To shed light on the structural signals that arise within
156 the microtubular lattice and their relevance for MAP recruitment, we have compiled this atlas. In
157 this work, we characterize the structural effects induced by different chemotypes from the two
158 major families of MSAs using fiber diffraction analyses of aligned MTs and computer simulations.
159 In parallel, through TIRFM (Total Internal Reflection Fluorescence Microscopy)-based assays, we
160 examine how these structural alterations influence the interaction of two key MAPs, tau and
161 kinesin, with the modified filaments. This integrated knowledge provides the microtubule
162 community with the tools to chemically manipulate MT structure at will, offering new opportunities
163 to unravel the principles governing MT regulation and to design safer and more potent tubulin-
164 targeting agents.
165
166 **Results.**
167 ***Fiber diffraction analysis of chemically stabilized microtubules.***
168 Previous studies from our group demonstrated the strong influence of paclitaxel (21, 33,
169 34) and other taxanes (21, 35, 36) on MT structure, inducing both alterations in the number of
170 PFs of the polymer and, as a common feature, an expansion of the MT lattice reflecting a change
171 in the helical pitch from 4.06 nm to 4.17 nm. Such an expansion has been previously observed in
172 hyper-stabilized MTs assembled in the presence of the slowly hydrolysable nucleotide analog
173 GMPCPP (37-39) as well as in catalytically inactive αE254A and αE254N MTs (40). This finding
174 led to the hypothesis that expansion was linked to the activated state of tubulin despite the fact
175 that both GMPPCP and metal fluoride (BeF_3^- and AlF_4^-) stabilized MTs in the compressed state
176 (34). Moreover, doubly activated paclitaxel- and BeF_3^--bound MTs are also in the compressed
177 state (34) and this expansion can be induced by the otherwise biochemically and cellular inactive
178 baccatin III (a precursor of paclitaxel biosynthesis lacking the C-13 side chain) (21). This suggests
179 that the observed lack of compression in GMPCPP and in the catalytically inactive MTs is due to
180 the inability of the catalytic residue Gluα254 to interact with the γ-phosphate,

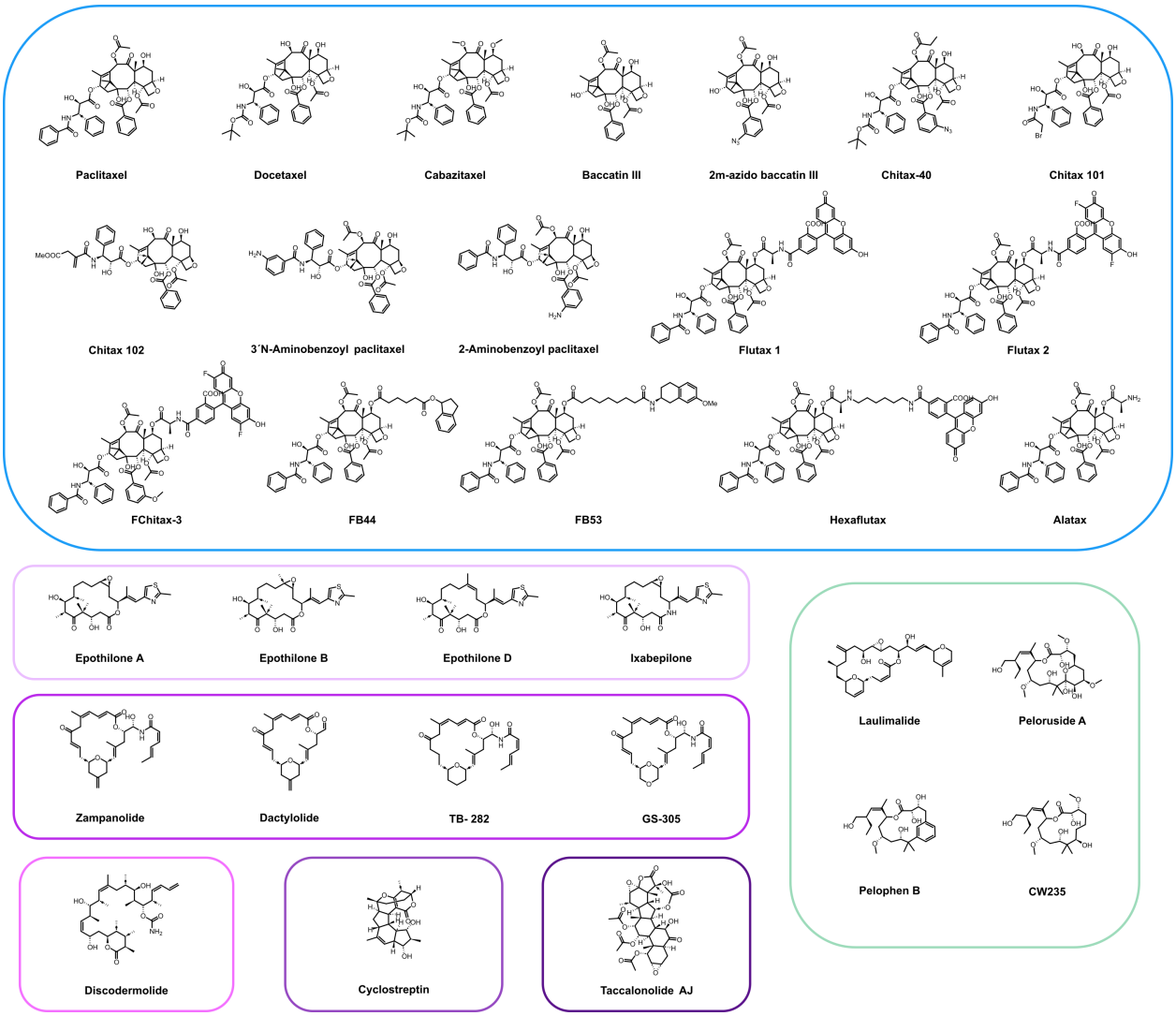

Figure 1. Chemical structures of the MSAs employed in the study.

either because of the geometric restraints imposed by GMPCPP or as a result of the amino acid replacement.

In order to understand the molecular mechanisms that determine the structural regulation of MTs by chemicals able to stabilize them we employed fiber diffraction of aligned MT samples (41) to determine their structural parameters (**Table I**) in the presence of a library of MSAs (**Figure 1**) covering a variety of chemotypes of both taxane and peloruside/laulimalide sites, including taxanes, epothilones, discodermolide, zampanolides, taccalonolide, cyclostreptin, as well as different pelorusides (including synthetic analogs) and laulimalide. Those conditions already published by our group (21, 25, 34, 42) were re-measured and/or re-analyzed to ensure an exact comparison between all figures presented.

Drug	J_{02}[1]	Radius[2]	Avg PF num[3]	1 nm^{-1} band	Avg monomer rise	State[4]
Non drug-stabilized MTs						
Apo	0.0892 ± 0.0001	11.72 ± 0.01	12.91 ± 0.02	0.987 ± 0.001	4.05 ± 0.01	C
GMPCPP	0.0883 ± 0.0003	11.83 ± 0.04	13.05 ± 0.04	0.960 ± 0.001	4.17 ± 0.01	E
GDP·BeF_3^-	0.0935 ± 0.0001	11.18 ± 0.01	12.32 ± 0.01	0.979 ± 0.007	4.08 ± 0.03	C
GDP·AlF_4^-	0.0908 ± 0.0005	11.51 ± 0.06	12.69 ± 0.07	0.986 ± 0.001	4.05 ± 0.03	C
Taxanes						
PTX	0.0937 ± 0.0002	11.15 ± 0.03	12.29 ± 0.03	0.958 ± 0.001	4.17 ± 0.02	E
PTX+CPP	0.0918 ± 0.0004	11.38 ± 0.05	12.54 ± 0.05	0.955± 0.003	4.18 ± 0.02	E
PTX+BeF_3^-	0.0923 ± 0.0001	11.32 ± 0.01	12.48 ± 0.05	0.994± 0.003	4.03 ± 0.03	C
PTX+AlF_4^-	0.0918 ± 0.0002	11.38 ± 0.01	12.55 ± 0.03	0.991± 0.003	4.04 ± 0.02	C
DTX	0.0887 ± 0.0002	11.78 ± 0.03	12.99 ± 0.03	0.958± 0.001	4.17 ± 0.02	E
DTX+CPP	0.0881 ± 0.0004	11.86 ± 0.05	13.08 ± 0.06	0.958± 0.001	4.17 ± 0.01	E
CBTXL	0.0897 ± 0.0008	11.7 ± 0.1	12.8 ± 0.1	0.960± 0.001	4.16 ± 0.03	E
CBTXL+CPP	0.0888 ± 0.0008	11.8 ± 0.1	13.0 ± 0.1	0.961± 0.001	4.16 ± 0.02	E
BIII	0.0978 ± 0.0001	10.68 ± 0.01	11.78 ± 0.01	0.958± 0.001	4.17 ± 0.01	E
BIII+CPP	0.0965 ± 0.0002	10.83 ± 0.02	11.94 ± 0.02	0.958± 0.001	4.18 ± 0.02	E
Azido-BIII	0.0983 ± 0.0003	10.63 ± 0.03	11.71 ± 0.04	0.960± 0.001	4.17 ± 0.01	E
Azido-BIII+CPP	0.0966 ± 0.0003	10.82 ± 0.03	11.92 ± 0.02	0.960± 0.001	4.17 ± 0.01	E
CTX40	0.0909 ± 0.0004	11.50 ± 0.05	12.67 ± 0.06	0.958± 0.001	4.18 ± 0.01	E
CTX40+CPP	0.0942 ± 0.0002	11.09 ± 0.02	12.23 ± 0.03	0.958± 0.001	4.18 ± 0.01	E
CTX101	0.0911 ± 0.0003	11.47 ± 0.04	12.64 ± 0.04	0.950± 0.004	4.21 ± 0.02	E
CTX102	0.0913 ± 0.0002	11.45 ± 0.02	12.62 ± 0.03	0.960± 0.001	4.16 ± 0.01	E
CTX102+CPP	0.0905 ± 0.0006	11.55 ± 0.08	12.73 ± 0.09	0.958± 0.001	4.17 ± 0.01	E
3´N-PT	0.0937 ± 0.0005	11.15 ± 0.06	12.29 ± 0.07	0.956± 0.002	4.18 ± 0.01	E
2-AB-PT	0.0925 ± 0.0003	11.30 ± 0.04	12.45 ± 0.04	0.957± 0.001	4.18 ± 0.01	E
2-AB-PT+CPP	0.0882 ± 0.0006	11.85 ± 0.08	13.06 ± 0.09	0.960± 0.006	4.17 ± 0.03	E
FTX1	0.0817 ± 0.0001	12.79 ± 0.02	14.10 ± 0.02	0.989± 0.001	4.04 ± 0.01	C
FTX1+CPP	0.0809 ± 0.0002	12.91 ± 0.03	14.24 ± 0.04	0.960± 0.001	4.16 ± 0.01	E
FTX2	0.0816 ± 0.0004	12.81 ± 0.06	14.12 ± 0.07	0.986± 0.001	4.06 ± 0.01	C
FTX2+CPP	0.0806 ± 0.0002	12.97 ± 0.03	14.29 ± 0.04	0.958± 0.001	4.17 ± 0.01	E
FCH3	0.0807 ± 0.0002	12.96 ± 0.03	14.27 ± 0.04	0.983± 0.001	4.07 ± 0.01	C
FB44	0.0831 ± 0.0004	12.58 ± 0.06	13.86 ± 0.05	0.986± 0.004	4.06 ± 0.02	C
FB44+CPP	0.0816 ± 0.0003	12.80 ± 0.05	14.11 ± 0.05	0.958± 0.002	4.17 ± 0.01	E
FB53	0.0877 ± 0.0002	11.92 ± 0.03	13.13 ± 0.03	0.987± 0.002	4.05 ± 0.01	C
FB53+CPP	0.0886 ± 0.0003	11.79 ± 0.04	13.00 ± 0.04	0.97± 0.01	4.12 ± 0.04	B
HXFTX	0.0824 ± 0.0001	12.68 ± 0.02	13.98 ± 0.02	0.99± 0.01	4.06 ± 0.01	C
HXFTX+CPP	0.0785 ± 0.0001	13.31 ± 0.02	14.67 ± 0.02	0.963± 0.002	4.15 ± 0.05	B
ATX	0.085 ± 0.003	12.3 ± 0.5	13.6 ± 0.5	0.988± 0.001	4.05 ± 0.01	C
ATX+CPP	0.0889 ± 0.0003	11.75 ± 0.04	12.96 ± 0.04	0.958± 0.001	4.18 ± 0.01	E

Table Ia. Structural parameters of microtubules in the presence of taxanes.

1.- nm^{-1}.
2.- nm as calculated from J_{02}=1.045/R.
3.- Calculated from an interprotofilament mean distance of 5.7 nm(35).
4.- C Compressed, E Expanded, B Blurred.
Abbreviations employed (see Figure 1): PTX: paclitaxel, DTX: docetaxel, CBTXL: cabazitaxel, BIII: baccatin III, Azido-BIII: 2m-azido-Baccatin III, CTX40: Chitax 40, CTX101: Chitax 101, CTX102: Chitax 102, 3'N-PT: 3´-aminobenzoyl paclitaxel, 2-AB-PT: 2-aminobenzoyl paclitaxel. FTX1: Flutax 1; FTX2: Flutax 2; FCH3: FChitax 3. HXFTX: Hexaflutax. ATX: alanylpaclitaxel.

Drug	J_{02}[1]	Radius[2]	Avg PF num[3]	1 nm^{-1} band	Avg monomer rise	State[4]
Epothilones						
Epo A	0.0939 ± 0.0001	11.13 ± 0.01	12.27 ± 0.01	0.960 ± 0.01	4.17 ± 0.01	E
Epo A+CPP	0.0931 ± 0.0004	11.22 ± 0.05	12.37 ± 0.05	0.959 ± 0.01	4.17 ± 0.01	E
Epo B	0.0910 ± 0.0002	11.48 ± 0.03	12.65 ± 0.03	0.962 ± 0.002	4.16 ± 0.01	E
Epo B+CPP	0.0923 ± 0.0005	11.32 ± 0.06	12.48 ± 0.07	0.963 ± 0.002	4.16 ± 0.01	E
Epo D	0.0926 ± 0.0003	11.29 ± 0.04	12.44 ± 0.04	0.966 ± 0.006	4.15 ± 0.03	E
Epo D+CPP	0.0926 ± 0.0004	11.29 ± 0.05	12.44 ± 0.05	0.957 ± 0.004	4.18 ± 0.02	E
IBP	0.0930 ± 0.0001	11.24 ± 0.01	12.39 ± 0.01	0.961 ± 0.001	4.16 ± 0.01	E
IBP+CPP	0.0913 ± 0.0008	11.4 ± 0.1	12.6 ± 0.1	0.960 ± 0.001	4.17 ± 0.01	E
Zampanolides						
ZMP	0.0793 ± 0.0002	13.17 ± 0.03	14.52 ± 0.04	0.988 ± 0.001	4.05 ± 0.02	C
ZMP+CPP	0.0785 ± 0.0002	13.31 ± 0.03	14.67 ± 0.04	0.986 ± 0.001	4.06 ± 0.01	C
DCT	0.0888 ± 0.0001	11.77 ± 0.01	12.97 ± 0.01	0.959 ± 0.001	4.17 ± 0.01	E
DCT+CPP	0.0881 ± 0.0004	11.86 ± 0.05	13.08 ± 0.05	0.958 ± 0.001	4.17 ± 0.01	E
TB282	0.10 ± 0.01	10.5 ± 1.1	11.5 ± 1.3	0.987 ± 0.001	4.05 ± 0.01	C
TMA282+CPP	0.0803 ± 0.0001	13.01 ± 0.02	14.35 ± 0.02	0.97 ± 0.01	4.12 ± 0.05	B
GS305	0.0793 ± 0.0001	13.18 ± 0.02	14.53 ± 0.02	0.987 ± 0.001	4.05 ± 0.01	C
GS305+CPP	0.0784 ± 0.0001	13.33 ± 0.02	14.69 ± 0.02	0.982 ± 0.007	4.07 ± 0.01	B
Discodermolide						
DDM	0.089 ± 0.003	11.7 ± 0.4	12.9 ± 0.4	0.988 ± 0.003	4.05 ± 0.02	C
DDM+CPP	0.0900 ± 0.0008	11.6 ± 0.1	12.8 ± 0.1	0.990 ± 0.003	4.04 ± 0.02	C
Cyclostreptin						
CSTR	0.0888 ± 0.0002	11.77 ± 0.03	12.97 ± 0.03	0.987 ± 0.001	4.05 ± 0.01	C
Taccalonolide						
TACCA-AJ	0.0902 ± 0.0002	11.58 ± 0.03	12.77 ± 0.03	0.987 ± 0.001	4.05 ± 0.01	C
Peloruside/Laulimalide						
LAU	0.0838 ± 0.0002	12.47 ± 0.03	13.75 ± 0.03	0.990 ± 0.003	4.04 ± 0.02	C
LAU+CPP	0.0842 ± 0.0002	12.41 ± 0.03	13.68 ± 0.03	0.97 ± 0.01	4.12 ± 0.05	B
PLA	0.0965 ± 0.0002	10.83 ± 0.03	11.94 ± 0.03	0.987 ± 0.001	4.05 ± 0.01	C
PLA+CPP	0.0981 ± 0.0004	10.65 ± 0.05	11.74 ± 0.05	0.958 ± 0.001	4.17 ± 0.01	E
PPH	0.0890 ± 0.0002	11.74 ± 0.03	12.94 ± 0.03	0.987 ± 0.001	4.05 ± 0.01	C
PPH+CPP	0.0906 ± 0.0001	11.53 ± 0.02	12.71 ± 0.02	0.959 ± 0.001	4.17 ± 0.01	E
CW235	0.0878 ± 0.0003	11.90 ± 0.04	13.12 ± 0.04	0.987 ± 0.001	4.05 ± 0.01	C
CW235+CPP	0.0872 ± 0.0002	11.98 ± 0.03	13.21 ± 0.03	0.958 ± 0.001	4.17 ± 0.01	E
Co-stabilized MTs						
PTX+LAU	0.0857 ± 0.0002	12.19 ± 0.03	13.44 ± 0.03	0.958 ± 0.001	4.17 ± 0.01	E
PTX+PLA	0.1002 ± 0.0003	10.42 ± 0.03	11.50 ± 0.03	0.954 ± 0.001	4.19 ± 0.01	E

Table Ib. Structural parameters of microtubules in the presence of other taxane and peloruside/laulimalide site ligands.
1.- nm^{-1}.
2.- nm as calculated from J_{02}=1.045/R.
3.- Calculated from an interprotofilament mean distance of 5.7 nm (35).
4.- C: compressed, E: expanded, B: blurred.
Abbreviations employed (see Figure 1): Epo: epothilone, IBP: ixabepilone, DDM: discodermolide, ZMP: zampanolide, DCT: dactylolide, CSTR: cyclostreptin; TACCA-AJ: taccalonolide AJ, LAU: laulimalide, PLA: peloruside A. PPH: pelophen B.

219 As expected from previous results (21, 33-36), ligand binding to both MSAs sites strongly
220 influences MT structure. From the images (**Figure 2**) obtained we can determine two different
221 clear effects on MT structure. The first and easier to interpret change occurs in the spacing of the
222 layer lines: in the presence of ligands, a new set of layer lines not visible in apo MTs can be easily
223 noticed at a spacing of 8 nm^{-1} from the equator, arising from the new 8 nm helix defined by ligand
224 binding to the MT lattice. Secondly, it can be noticed that, in the presence of some of the ligands,
225 the 4 nm^{-1} layer lines are displaced inwards, indicating that the microtubular lattice is expanded.
226 Interestingly, such expansion occurs asymmetrically and this allows to distinguish between α- and
227 β-tubulin as the set of layer lines at 8 nm^{-1} can also be noticed in the images. Interestingly, only
228 two possible dimer rise distances (4.06 or 4.17 nm) are possible, indicating two interchangeable
229 lattice spaces. It is worth noting that certain combinations of a drug stabilizing the compressed
230 state with GMPCPP result in blurred layer lines at intermediate spacings, which is indicative of
231 inhomogeneous lattices. This lattice expansion has been previously described upon binding of
232 paclitaxel and derivatives (34, 43), i.e., upon paclitaxel binding, the distance between α1- and β2-
233 tubulin subunits of two longitudinally aligned, concatenated tubulin dimers increases by roughly
234 2 Å relative to the unbound MT.
235 From the data obtained it can be noted that all taxanes, except those modified in C-7 (42),
236 and epothilones, induce lattice expansion. On the other hand, discodermolide, zampanolide,
237 cyclostreptin and taccalonolide AJ are able to stabilize MTs without having any effect on the
238 longitudinal spacing of the lattice, in common with compounds targeting the laulimalide/peloruside
239 site (e.g., laulimalide, peloruside A, pelophen B and CW235), and are in agreement with previous
240 results (25). These results indicate that it is also possible to stabilize MTs through the taxane site
241 without expanding them.
242 Another clear effect observed upon MT stabilization by MSAs bound at the taxane site is
243 the change in the position and shape of the J_0 maxima in the equator of the diffraction image.
244 Such changes indicate that binding to the taxane site influences lateral IPF interactions as it has
245 been previous described, both for the taxane site (33, 35) and the laulimalide/peloruside site (25).
246 However, although these results are concordant with previous studies—because paclitaxel
247 reduces the mean MT diameter while docetaxel keeps the MT diameter unaltered (33, 35)—it is
248 not straightforward to rationalize the observed changes.
249 From close examination of the fiber diffraction images the following facts can be deduced.
250 Firstly, as expected the position of the J_n peak remains unaltered, since it arises from the IPF
251 space and ligand binding is not expected to significantly alter the PF shape. Secondly, as a
252 general tendency those compounds that expand the microtubular lattice usually reduce or retain
253 the PF number, with baccatin III decreasing the MT radius to 10.32 ± 0.04 nm (average 11.38 ±
254 0.05 PFs). However, MSAs that do not expand the MT lattice do increase the MT radius; e.g.,
255 zampanolide increases the MT radius to 13.32 ± 0.04 nm (average 14.68 ± 0.05 PFs). Other
256 combinations of drugs with GMPCPP allow the generation of wider MTs with an expanded lattice.

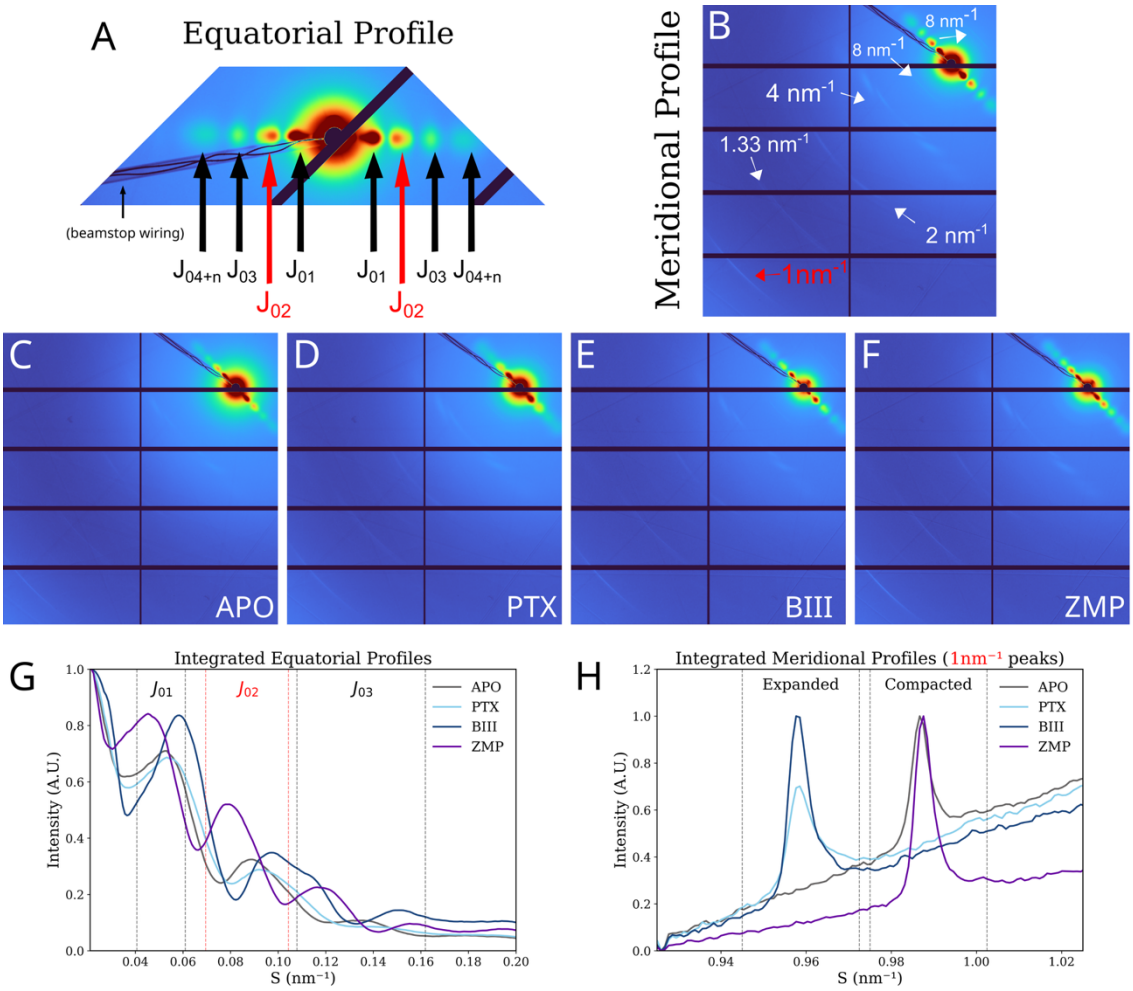

Figure 2. Interpretation of microtubule diffractograms. A. Reference image illustrating equatorial signal interpretation and Bessel peaks positions. **B.** Reference image illustrating meridional signal interpretation and layer lines localizations. **C–F**. Representative diffractograms for four microtubule conditions: (C) APO (gray), (D) PTX (light blue), (E) BIII (green), and (F) ZMP (purple). **G.** Azimuthally integrated equatorial profiles from the diffractoACams above, including theoretical ranges for Bessel J_0 peak positions corresponding to microtubules with radii between 10 and 15 nm. **H.** Azimuthally integrated meridional profiles focused on the 1 nm^{-1} layer line, highlighting the ranges associated with compacted and expanded lattice states.

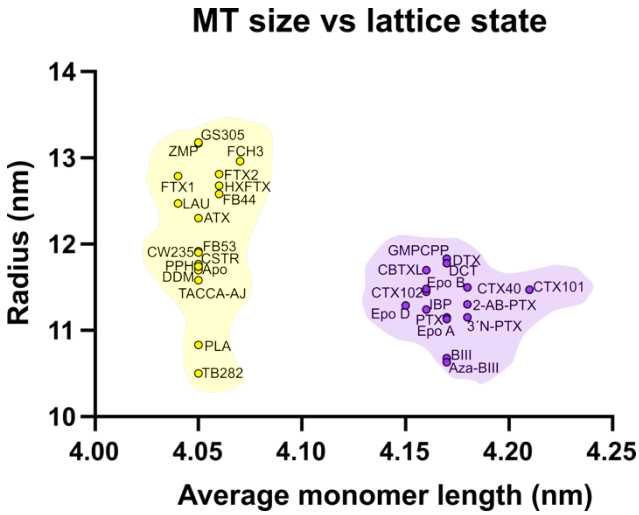

Figure 3. Relationship between the MT lattice state and MT radius for all the measured conditions.

Stoichiometry of the taxane site regulation of the microtubule structure.

Having demonstrated that the occupancy of the paclitaxel site results in changes in the microtubular lattice both in the longitudinal and the lateral directions, we aimed to understand the stoichiometry needed to produce this effect (**Figure 4**) to learn the possible responses of axonal MTs to different drug concentrations. We selected five taxane-site compounds, three of which are in clinical use (paclitaxel, docetaxel and ixabepilone), another taxane engineered to be fluorescent by a small modification at the C-13 side chain (3'N-PT), and the covalent binder zampanolide. Paclitaxel, ixabepilone, and 3'N-PT expand the lattice in the longitudinal direction while altering the IPF contacts which results in the loss of one PF on average (**Table I**); docetaxel changes only the longitudinal spacing while zampanolide, a compound inducing a compressed lattice, was tested on GMPCPP-bound pre-expanded MTs.

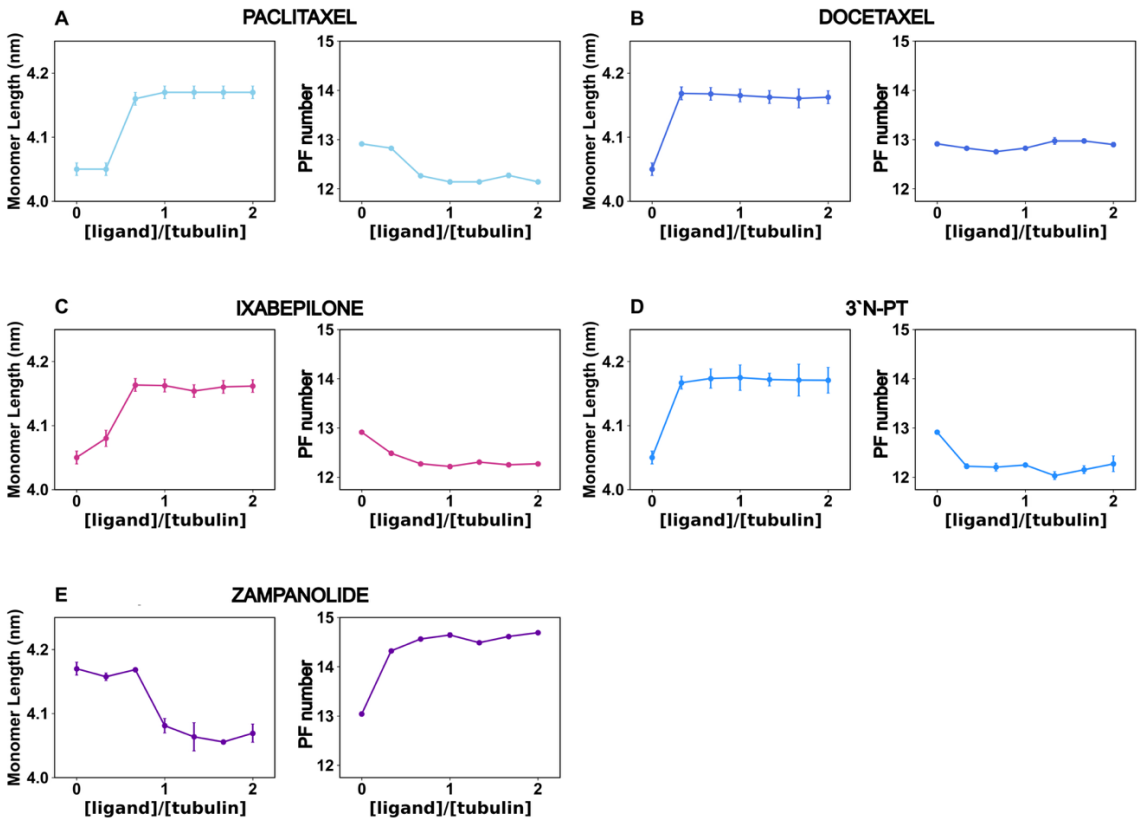

Figure 4. Structural response of microtubules to different ligand:tubulin ratios. The plots show the variation in average monomer length and protofilament number, highlighting the impact of ligand concentration on lattice organization. (A) paclitaxel, (B) docetaxel, (C) ixabepilone, (D) 3´aminobenzoyl paclitaxel, (E) zampanolide.

Remarkably, MTs are sensitive to the presence of substoichiometric concentrations of drugs, i.e., all drugs are able to induce the structural transition towards its equilibrium state (those obtained in fully bound MTs) at low saturation rates. Noticeable, transitions in both the longitudinal and lateral directions behave as an almost all-or-nothing principle. Concerning the longitudinal space transition, docetaxel- and 3'N-PT-bound MTs are expanded at the lowest stoichiometry of the drug tested (0.33); paclitaxel and ixabepilone induced expansion as well, whereas

zampanolide induced re-compression of the GMPCPP expanded lattice at the 0.33–0.66 stoichiometry range.

Time-resolved fiber diffraction analysis of the structural effect of chemical stabilization of microtubules induced by MSAs.

Once we examined the stoichiometry required to promote structural changes on MTs, we investigated the ability of the MT to react to changes in the chemical composition of the environment (**Supp. Movie 1**). To this end, we examined how three taxanes—docetaxel (PF-neutral) and the thinner MT promoters paclitaxel and baccatin III—affect pre-formed MT lattices, compared with laulimalide, an MSA that increases PF number without altering the axial tubulin repeat (25).

Previous reports on time-resolved measurements of the mean diameter of non-aligned MTs indicate that the change in diameter in response to the addition of paclitaxel or docetaxel occurs within the dead time of the technique, i.e., 30 s (44) (note that our shear flow and mixing system allows a time resolution of 1 s). Our findings presented in **Figure 5** reveal that upon addition of paclitaxel, docetaxel or baccatin III, the axial expansion of the MT takes place in less than 1 s. The consistency of this result is suggestive of a flexible lattice that is able to rapidly expand in response to the occupation of the taxane site by an expanding drug. The control experiment in the presence of the non-expanding MSA laulimalide shows no change upon drug addition (**Figure 5D**).

On the other hand, modification of the lattice in the lateral direction is, although slower in concordance with previous reports (44), far less extensive (at least in the early stages) than expected from the static measurements. Paclitaxel-induced microtubules contained, on average, 0.6 fewer PFs than those assembled in the absence of the drug. However, only a reduction of 0.3 PFs was observed during the first 3 s of measurement. Prolonged exposure (30 min) of preassembled microtubules to superstoichiometric concentrations of paclitaxel resulted in MTs apparently identical to those assembled in the continuous presence of the drug.

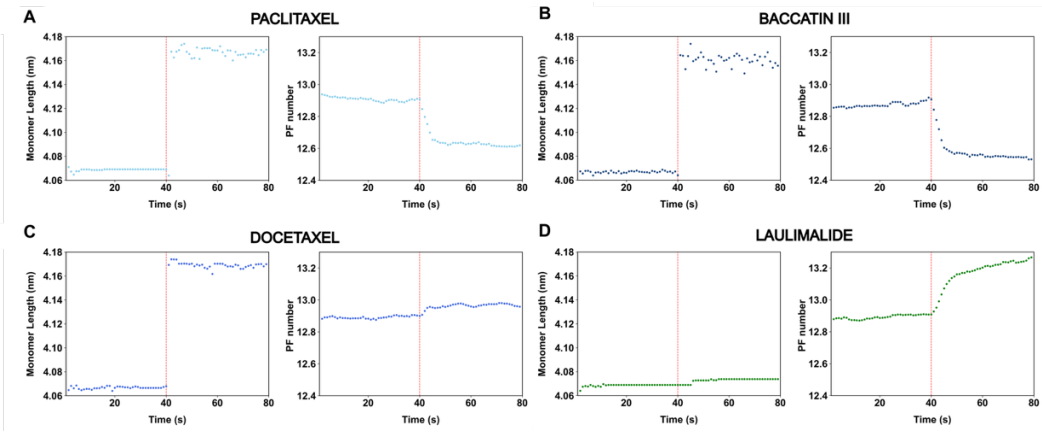

Figure 5. Time-resolved axial and radial measurements reveal different dynamics of microtubule lattice reorganization after ligand addition at 40 s (red dashed line). Left: average axial tubulin repeat. Right: average protofilament number. Ligands: (A) paclitaxel, (B) docetaxel, (C) baccatin III, (D) laulimalide.

Baccatin III is the compound that promotes a larger modification in the IPF contacts with a net loss of 1.1 PF. Similarly, for paclitaxel only a minor change of 0.3 PF was observed immediately after addition.

Finally, adding laulimalide to pre-formed MTs was neutral for the dimer length, as expected from previous results (25), and induced a net increment of 0.3 PF. Note that laulimalide generates MTs with an average of 1 extra PF compared with the apo ones. In all cases shown the time-resolved experiments revealed a fast small change in the PF number, indicating that the equilibrium in this parameter takes place in a longer time scale.

'In silico' model building and simulation.

To understand the structural mechanisms responsible for taxane site ligands modulation of the MT lattice and GTPase activation we next used computational modeling and molecular dynamics (MD) simulations. Our aims were to study (i) the low-frequency motions involved in the cooperative structural fluctuations leading to PF number variation in MTs, (ii) the conformational behavior of a set of representative drug-free and drug-bound (docetaxel, epothilone A, zampanolide, discodermolide and alatax) β1:α2 interfaces from MTs differing in interdimer rise and PF number, and (iii) the dynamics of a series of minimalist representations of MT lattices (45) made up of three laterally associated PF fragments, each consisting of a dimer of αβ-tubulin dimers. The results obtained allowed us to build several instances of representative full MT turns with both compacted and expanded drug-bound lattices that are now publicly available from the ModelArchive repository (46) (codes are listed in the Materials & Methods section).

The normal mode analyses performed on the 3´2 patches of tubulin dimers from 13- and 14-PF MTs consistently showed that the first non-trivial mode corresponds to a collective motion that can nicely explain the large-amplitude, slow-bending motion that drives the cooperative structural fluctuations justifying the observed PF number variation (**Supp. Movie 2**). By saving the coordinates of the model corresponding to the maximum amplitude, we obtained a suitable template for an [(α1:β1-α2:β2)/(α1':β1'-α2':β2')/(α1":β1"-α2":β2")] MT patch with either a slightly higher or a slightly lower degree of closure that led, upon careful energy refinement, to MTs consisting of 12 and 15 PFs, respectively.

Comparison of the β1:α2 interfaces in the presence of either GTP (pre-hydrolysis state) or GDP (post-hydrolysis state) in the β subunit clearly showed the expected direct interactions between the γ-phosphate of the former and the T3 loop in place of the water-mediated interactions with the β-phosphate in the latter. In addition, the simulations revealed a pleomorphic interface that can subtly change in response to environmental cues, including the presence of magnesium ions and the degree of solvation, which can give rise to distinct and easily interconvertible hydrogen-bonding patterns that subtly modulate not only the lattice parameters but also the water network and the torsion angles of the nucleotide distal phosphates (**Figure 6**). Most notably, the Aspβ179 residue in the ^{177}VSDTV^{181} stretch from the T5 loop, which in the PF adopts the so-called "in" conformation (47) also found in the α-tubulin ^{177}VSTAV^{181} counterpart, can accept a hydrogen bond from the hydroxyl of Tyrβ224 (the first residue in H7 whose replacement by Phe

is known to promote the formation of straight tubulin oligomers, which are more efficient in initiating MT nucleation and elongation (47)), the ribose hydroxyls of GTP, the Lysα352 amino group, the backbone nitrogen of Valα353, and/or the sidechain carboxamide of Asnα329. The Lysα352 amino group can also form a strong ionic interaction with the catalytic carboxylate of Gluα254, which in turn can fixate the sidechain carboxamide of Asnβ101. This functionality allows the formation of hydrogen bonds not only with Thrβ180 in the T5 loop but also with Asnα258 across the interdimer interface; besides, in concert with the backbone amide nitrogen, the Asnβ101 carboxamide appears to be essential for orienting the γ-phosphate in the elusive conformation that is necessary for nucleophilic attack by the activated water molecule (**Figure 6**).

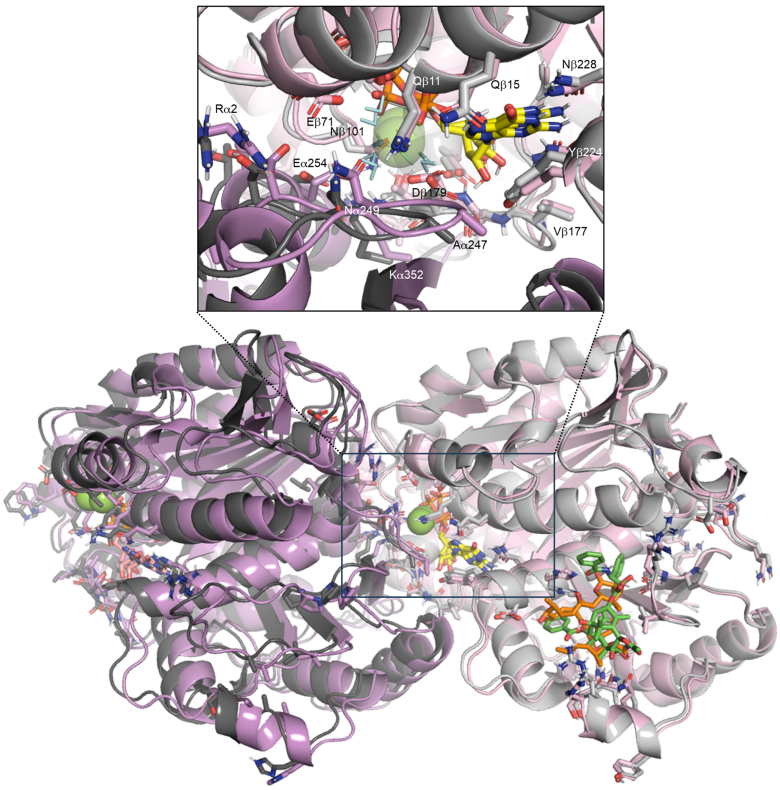

Figure 6. Overlay of the β1-α2 interfaces from a compressed PF (light and dark pink) with bound discodermolide (C atoms in orange) and an expanded PF (light and dark gray) with bound paclitaxel (C atoms in green) using only the β1 subunits for the root-mean-square superposition in PyMOL. The interdimer rise, measured as the distance between the centers of mass of the Cα atoms of β and α subunits, is 40.5 Å for the former and 42.0 Å for the latter. The C atoms of the GDP and GTP nucleotides are colored yellow and salmon, respectively, and the Mg^{2+} ions are displayed as green spheres. The boxed area appears enlarged at the top of figure to show the most notable interfacial differences and the hydrating water molecules (cyan thin sticks). Relevant residues explained in the text have been labeled.

Optimization of this intricate interplay is only achieved when the GTP cap matures and, as shown here, is amenable to modulation by MSAs bound at the taxane site. These bound ligands change the vibrational patterns and contribute to these conformational fluctuations in

389 slightly different ways depending on their chemical nature and the specific anchor residues
390 involved. The present results support the proposed crosstalk between the nucleotide- and taxane-
391 binding sites.
392
393 ***Effect of microtubule structure on nucleotide hydrolysis.***
394 Considering that MSAs are able to regulate the average monomer rise and the GTPase
395 activity at the E-site in β-tubulin, which is activated by the Gluα254 residue of the incoming tubulin
396 dimer (48), we aimed to investigate whether the modulation of the tubulin structure by MSAs is
397 reflected into differences in GTPase activity. To this end, we compared the GTPase activity of
398 MTs in the presence of a set of expanding (paclitaxel, epothilone A) and non-expanding ligands
399 bound to the taxane (discodermolide, zampanolide) or laulimalide/peloruside sites (pelophen B)
400 (25) relative to that of undrugged ones.
401 Firstly, we confirmed the GTPase activity of drugged MTs by analyzing the nucleotide
402 content of the assembled polymers. All drugged MTs were found to have 1 mole of GTP and 1
403 mole of GDP bound per tubulin dimer at one hour of incubation, indicating retention of GTPase
404 activity. Then, phosphate release was quantified using the malachite green inorganic phosphate
405 assay (49) (**Table II**). These results indicate, in concordance with previous reports (50), that
406 expansion reduces the kinetic rate of phosphate release by nearly 35%, while discodermolide
407 binding increases the hydrolysis rate by 45%.
408

Condition	Kinetic rate of phosphate release (min^{-1})
Apo (C)	0.11 ± 0.02
Paclitaxel (E)	0.07 ± 0.01
Epothilone A (E)	0.07 ± 0.02
Zampanolide (C)	0.11 ± 0.03
Discodermolide (C)	0.16 ± 0.02
Pelophen B (C)	0.10 ± 0.02

409
410 **Table II**. GTPase activity of drugged expanded and compressed microtubules. (C) compressed
411 and (E) expanded state of tubulin.
412
413 The finding that GTP hydrolysis is slower in expanded MTs (i.e., bound to paclitaxel or
414 epothilone A) and faster in MTs with bound discodermolide is indicative of an optimal alignment -
415 in the latter case of the Gluα254-activated water molecule that performs the nucleophilic attack
416 on the γ-phosphate to cleave the bond between the γ- and the β-phosphate (**Figure 6**). This
417 reaction has been deemed to be, on theoretical grounds (51), extremely sensitive to the
418 geometrical features of the site and this assertion is confirmed by the present results, which show
419 that activation of GTP hydrolysis at the E-site is distinctly regulated by ligands. Intriguingly, binding
420 of the pseudocyclic discodermolide—despite its deceitfully greater conformational freedom on
421 paper relative to its macrocyclic congeners, e.g., dictyostatin)—displays an unusual favorable
422 entropic contribution to the binding free energy (52). On the basis of our MD simulation results for
423 both the free and bound forms, we posit that its high binding affinity for tubulin is achieved by

424 significant conformational restraints—mostly due to the distinct distribution of double bonds—that
425 pre-shape this ligand to exhibit excellent shape and electrostatic complementarity with the taxane
426 binding site on the β-tubulin subunit of straight PFs without incurring in strain and entropic
427 penalties. Furthermore, the hydroxyl groups that point outward interact, in a very precise fashion,
428 with both donor/acceptor groups in the taxane binding pocket, and also with some water
429 molecules. This binding signature is unique to discodermolide, as it involves the side chains of
430 Aspβ226 and Hisβ229 in helix H7, the backbone nitrogen of Thrβ276, the backbone carbonyl of
431 Argβ369 in the T9 hairpin and the carboxamide group of Glnβ281 in the M loop. As a result of the
432 vibrational changes brought about by this anchoring, the bound drug elicits an allosteric effect on
433 the conformation of the GTP phosphates at the E-site such that the attack by the Gluα254-
434 activated nucleophilic water molecule is facilitated and the interdimer rise shortening is promoted.
435 On the contrary, taxane and epothilone binding, by establishing a different well-described set of
436 interactions (21, 53), increase the interdimer rise distance and slow down the GTP hydrolysis rate
437 because they promote an alternative arrangement of the GTP phosphates that raises the energy
438 barrier that is necessary to overcome in order to stabilize the transition state of the reaction.
439
440 ***Effect of structural changes on chemical transport on microtubules.***
441 Kinesin-mediated chemical transport, crucial for neurotransmitters movement along the
442 axons, is one of the main cellular functions of microtubules (54). This transport relies on kinesin
443 recognition of the MT surface. Now that we have the tools to modulate MT structures, we aim to
444 understand how these structural changes affect kinesin motility.
445 To address this issue, we employed the time-lapse total internal reflection fluorescence
446 (TIRF) microscopy system described in our previous study (42). Using labeled kinesin motors
447 (Kif5B 1–905-eGFP (55)), we tracked and analyzed individual kinesin particles upon immobilized
448 MTs stabilized by a panel of distinct MSAs that produce different architectures, to characterize
449 several physical properties (**Figure 7 and Supp. Movie 3**) related with their function
450 (affinity -motors per unit MT length-, run length, interaction time, and average velocity). Data for
451 paclitaxel (expanded, reduced PF number), FB44 (compressed, increased PF number), FB53
452 (compressed, neutral PF number), and GMPCPP (expanded, neutral PF number) were taken
453 from our earlier work (42). We then selected four additional compounds targeting the taxane site—
454 docetaxel (expanded, neutral PF number), epothilone B (expanded, reduced PF number),
455 zampanolide (compressed, increased PF number), and discodermolide (compressed, neutral PF
456 number)—and three compounds targeting the peloruside/laulimalide site—peloruside A
457 (compressed, reduced PF number), laulimalide (compressed, increased PF number), and
458 pelophen B (compressed, neutral PF number).
459
460

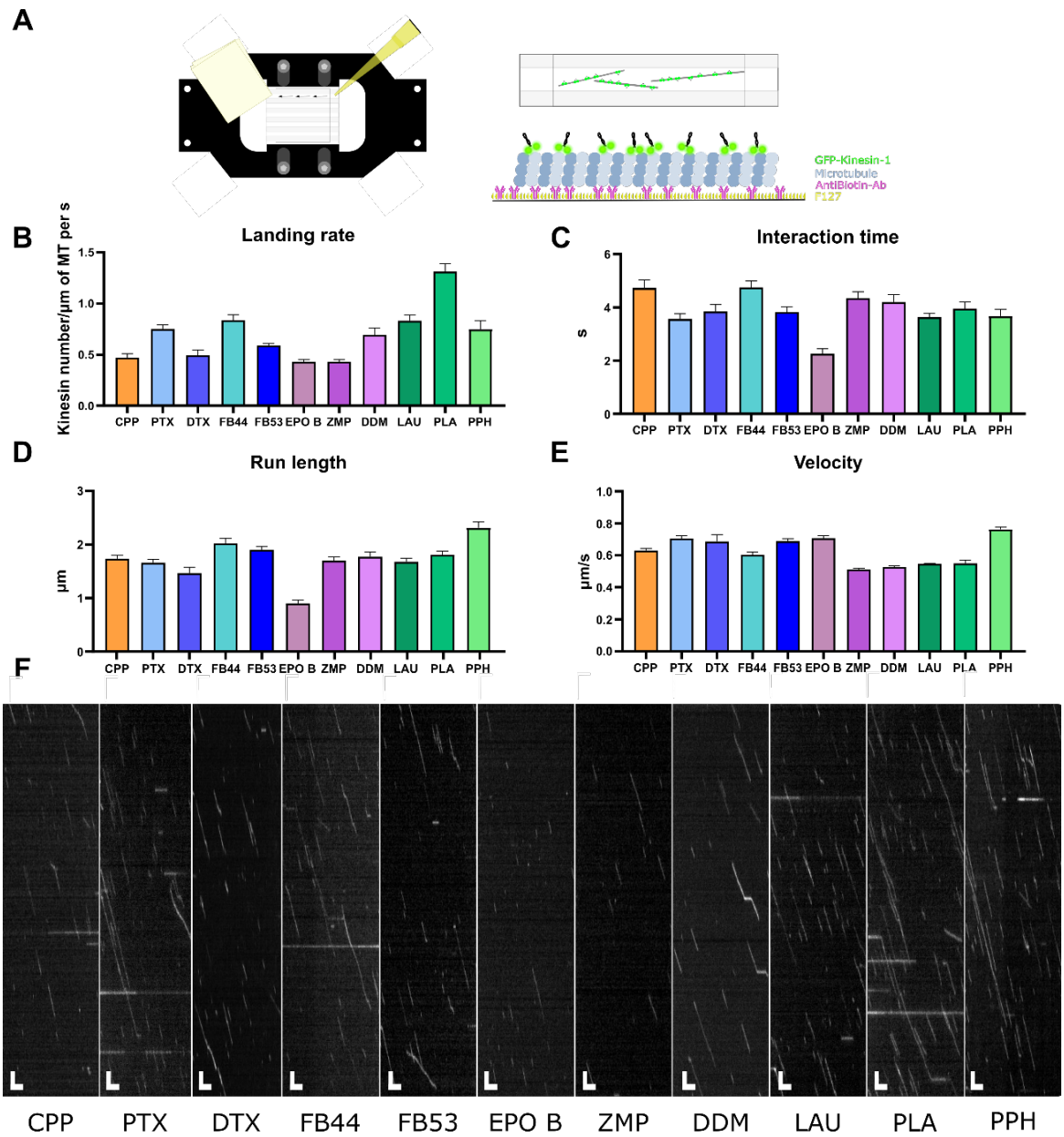

Figure 7. Characterization of kinesin motility. A. Schematic representation of the single-molecule kinesin motility assay. Stabilized microtubules (MTs) were immobilized in a pre-treated flow chamber, and 10.8 nM Kif5B-eGFP was added. The movement of individual motors was recorded using TIRF microscopy and subsequently analyzed. **B–E.** Scatter plots and quantitative summary from at least three independent experiments, showing (B) mean landing rate of kinesin (events/µm per s), (C) mean dwell time (s), (D) mean run length (µm), and (E) mean velocity (µm/s) of single Kif5B-eGFP molecules moving on stabilized MTs. Error bars represent the SEM. Data were pooled from ≥ 2 experiments per condition, analyzing between 36–48 MTs per replica. **F.** Representative kymographs of single Kif5B-eGFP motors moving along a stabilized microtubule. Vertical scale bar: 2 µm; horizontal scale bar: 10 s.

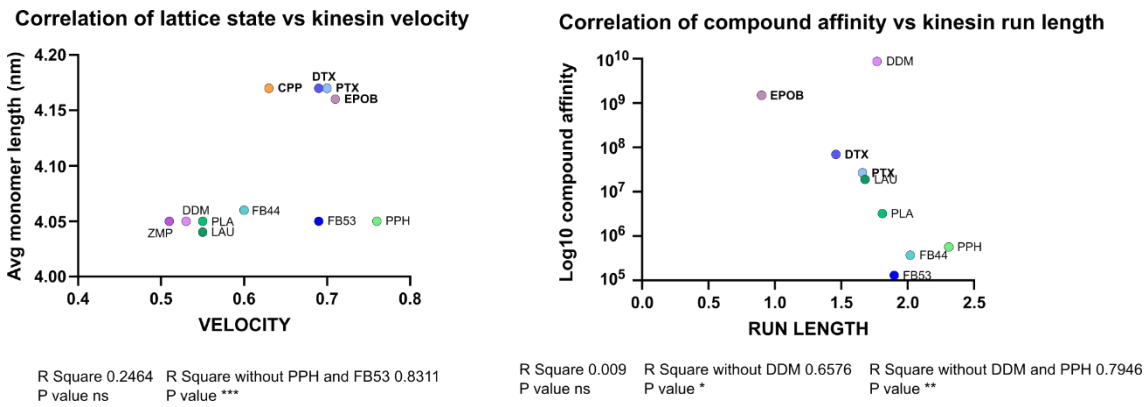

Figure 8. Statistical correlations found between the structural and affinity parameters of the drug-stabilized lattices and the interaction of kinesin with them. Pearson correlation was obtained using GraphPad Prism 8 software to determine R square and P value (**** $p < 0.0001$; *** $p < 0.001$, ** $p < 0.01$ and * $p < 0.05$).

Although the data presented here demonstrates a complex dependence of kinesin–MT interactions on the specific structural state induced by drug binding, overall, it confirms that ligand binding to MT alters kinesin interaction and motility. Hence, we have identified several consistent trends. Firstly, the velocity (**Figure 7E**) can be categorized as faster and slower, and correlates with the monomer length state (**Figure 8A**), being consistently faster on expanded lattices (as kinesin-decorated MTs are typically expanded) and on lattices stabilized by ligands with relatively low binding affinities (FB44, FB53, and PPH). In contrast, strongly stabilized compressed lattices yield slower motility. This may reflect that low binding affinity ligands poorly stabilize the compressed state, making kinesin binding induced expansion easier. Landing rate (**Figure 7B**) is reduced on expanded lattices and in the presence of zampanolide (which increases PF number). The interaction time (**Figure 7C**) is generally consistent across conditions, except for epothilone B, which produces significantly shorter dwell times. The run length (**Figure 7D**) is relatively stable across conditions, with two notable exceptions: epothilone B, which reduces run length, and PPH, which increases it. Interestingly, the run length correlates to some extent with the affinity of the assayed ligands (**Figure 8B**), suggesting that stronger stabilization of the microtubule impairs kinesin-movement-associated accommodation of the lattice during kinesin's functioning.

It is worth mentioning that epothilone B stands out as the only compound that strongly stabilizes an expanded lattice ($K_b = 1.5 \times 10^9\ M^{-1}$ at 26 °C). Despite kinesin moving at the same velocity on epothilone B-stabilized lattices, it binds with lower affinity and dissociates more rapidly compared to other conditions.

Effect of structural changes on tau binding and kinetics.

Tau is the most important MT modulator in axons, requiring a highly dynamic interaction with MTs to exert its stabilizing function (56). Failure of tau to interact with MTs leads to the formation of neurofibrillary tangles—typical of Alzheimer disease—in addition to the impaired stability of axonal MTs. In order to learn from the structural features influencing tau recognition by MTs, we employed the same drugs as kinesin binding assay to study the interaction of mCherry

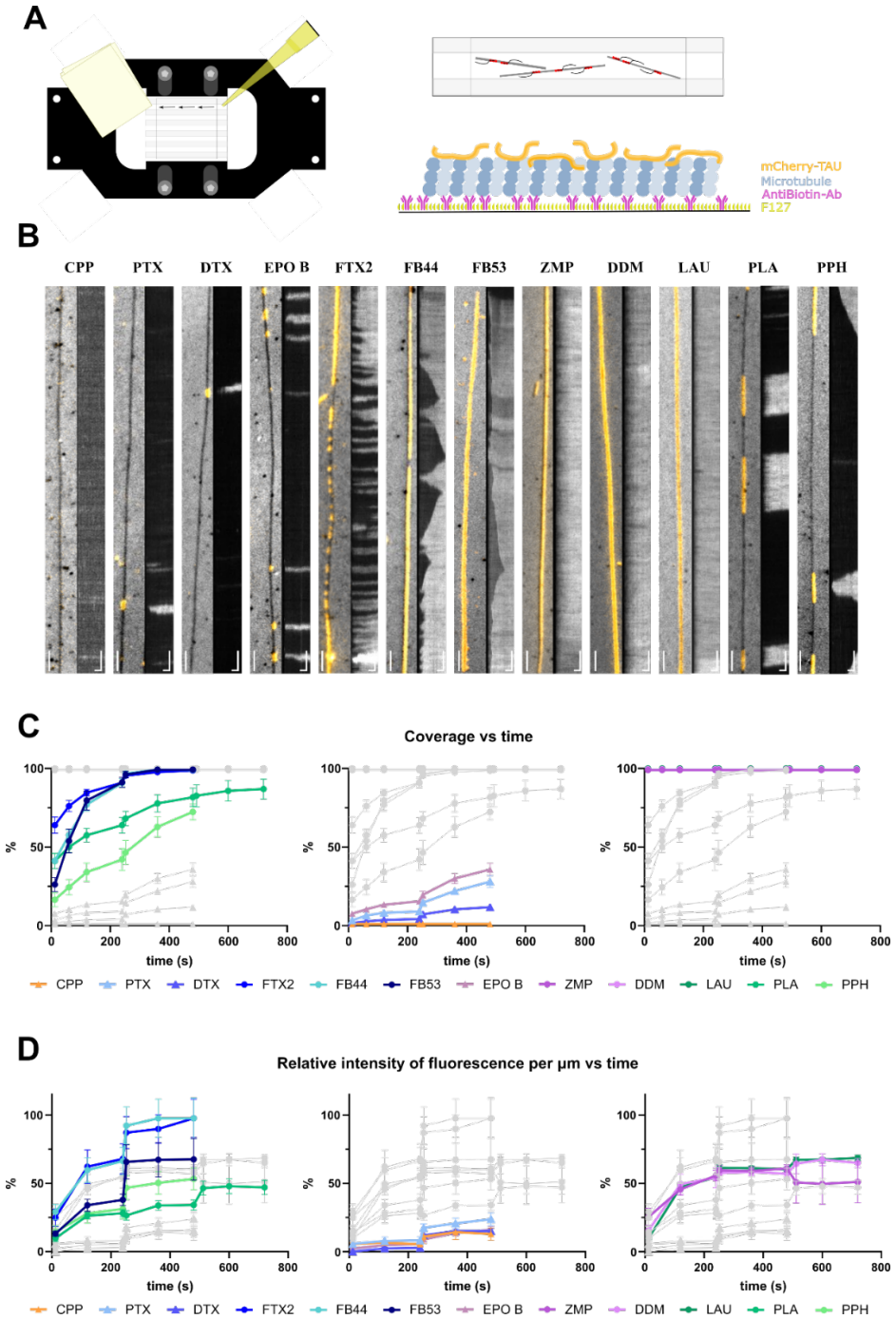

Figure 9. Characterization of tau interaction with microtubules. A. Schematic representation of the TIRF microscopy assay setup. Label-free stabilized microtubules (MTs) were immobilized on a pre-treated glass coverslip. Purified tau-mCherry was added, and its binding to MTs was recorded. Fluorescence intensity of tau-mCherry along each MT was measured and analyzed. **B.** Representative fluorescence images (after 4 minutes) and corresponding kymographs of tau-mCherry binding to MTs stabilized with GMPCPP or different drugs. Vertical scale bars: 2 µm; horizontal scale bars: 60 s. Taxol derivatives are shown in blue shades, other taxanes in purple tones, and peloruside/laulimalide site ligands in different greens. Triangle symbols indicate expanders; circle symbols represent non-expander compounds. **C.** Fraction of MT length covered by tau envelopes over time following tau-mCherry addition. **D.** Integrated fluorescence density per µm of MT over time after tau-mCherry addition.

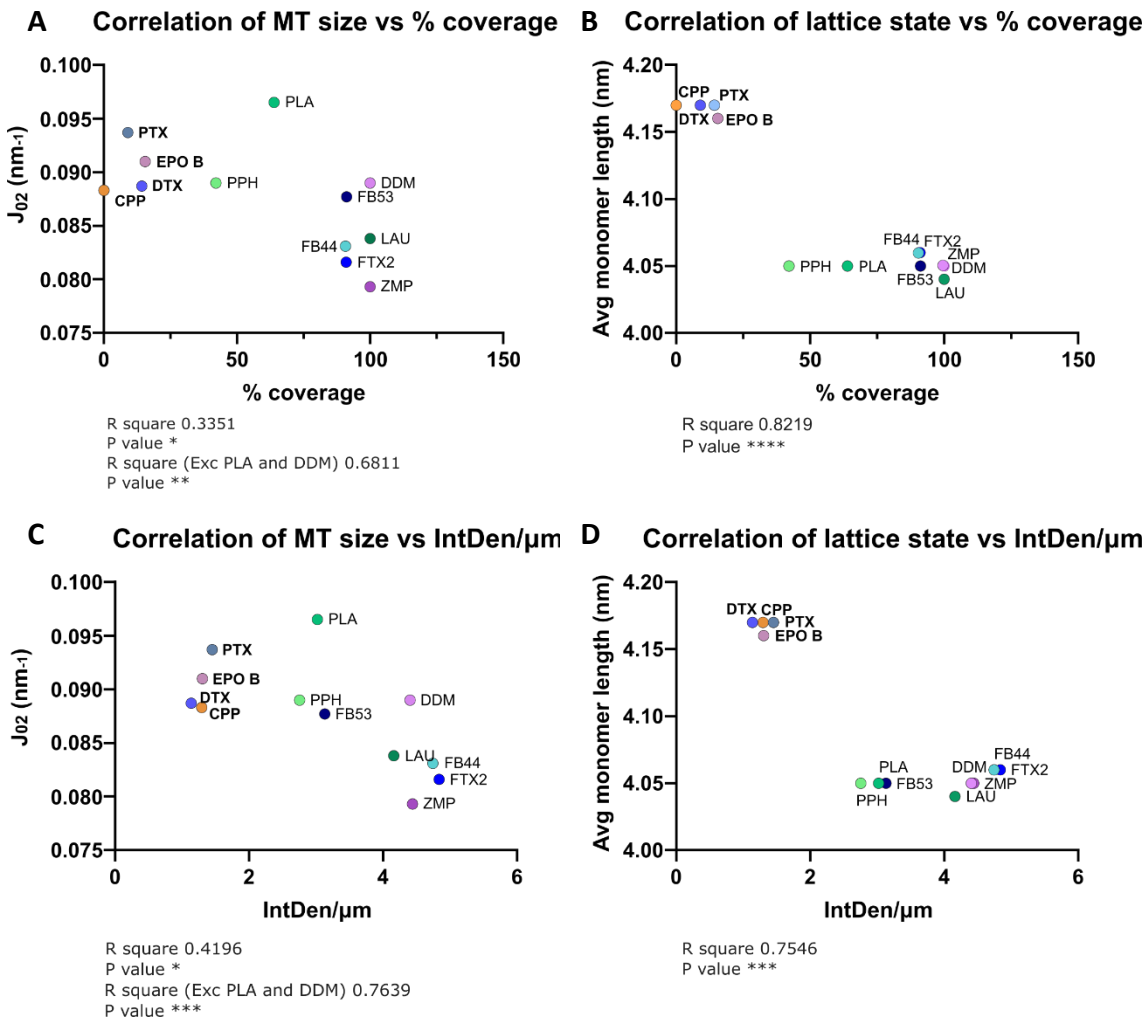

Figure 10. Statistical correlations found between the structural parameters of the drug stabilized lattices and the binding of tau to them. Pearson correlation was obtained using GraphPad Prism 8 software to determine R square and P value (**** $p < 0.0001$; *** $p < 0.001$, ** $p < 0.01$ and * $p < 0.05$).

labeled tau 441 isoform with immobilized stabilized MTs, using the same technique as we performed in our previous work (42).

We deposited the distinct ligand-bound stabilized MTs in a flow chamber and visualized them using total internal reflection microscopy. We then added 10 nM of tau-mCherry and monitored its association with MTs (**Figure 9A**). As for zampanolide, discodermolide, peloruside A and laulimalide, the standard tau concentration of 10 nM resulted in instantaneous binding that precluded any kinetic analysis we reduced the initial tau concentration to 5 nM to resolve whether tau binding occurred uniformly along the microtubule or binding proceed through patches that grow at an accelerated rate.

After 4 min, we increased the tau-mCherry concentration up to 10 nM for zampanolide, discodermolide, peloruside A and laulimalide and up to 40 nM for the rest of the ligands, recording its binding to MTs for another 4 min. Data for GMPCPP, paclitaxel, FB44 and FB53 are taken from(42).

541 The most relevant observation is that zampanolide-, discodermolide- and laulimalide-stabilized
542 MTs bind tau within the dead time of the technique (MTs are fully covered in 10 seconds) despite
543 the lower concentration of tau employed (5 nM instead of 10 nM), suggesting that these structures
544 are very easily recognized by tau (**Figure 9B**, **9C** and **Supp. Movies 4–6**) while GMPCPP MTs
545 are not covered, indicating that this lattice is not recognized by tau. Concerning the other
546 stabilized MTs, we observed that tau bound in patches which diffused along MTs expanding
547 progressively as previously described for tau binding to them (57). In good agreement with
548 previous results (42), expanded MTs (epothilone B- and docetaxel-bound) bind tau with rates
549 similar to those observed for paclitaxel-bound MTs (42), requiring times in the order of minutes to
550 significantly cover MTs (**Supp. Movies 7** and **8**). Although there is a clear correlation between
551 lattice expansion and tau binding (**Figure 10B** and **10D**), there are clear differences between
552 binding of tau to different non-expanded lattices. Zampanolide, discodermolide, and laulimalide
553 stabilized MTs within the dead time of the technique (fully covered in 10 s), peloruside A- and
554 pelophen B-stabilized MTs bind tau noticeably slower (**Supp. Movies 9** and **10**) (although faster
555 than expanded MTs), behaving similar to MTs stabilized by taxanes in which the expansive effect
556 had been removed by the addition of groups at C-7 position (42).
557 We also calculated the total amount of tau bound to the structures (**Figure 9D**) based on
558 the total fluorescence signal. The clear distinction in this measurement between expanded and
559 non-expanded lattices resembles the percentage of MT cover (**Figure 9B**). While expanded MTs
560 (paclitaxel, docetaxel and epothilone B) require 40 nM tau-mCherry and a long exposure time to
561 show an average fluorescence over the background, compacted lattices bind rapidly to reach a
562 full binding at lower times and concentrations. However, it is worth mentioning that although tau
563 covers all the zampanolide-, discodermolide- and laulimalide-stabilized MTs within the dead time
564 of the technique, with pelophen B and peloruside A showing slower binding kinetics, full binding
565 of tau is not immediate as the MT continuously increases fluorescence with time until it reaches
566 the maximum value.
567 Finally, it is not possible to find a strong correlation between MT diameter and tau binding,
568 albeit a weak correlation (with outliers) can be observed, inferring that thicker MTs allow to bind
569 a higher concentration of tau (**Figures 10A** and **10C**). Collectively, these observations together
570 with the evidence that tau affinity correlates with lattice state, are consistent with fact that MTs
571 stabilized by expanding drugs are thinner than those stabilized by non-expanding drugs (see
572 above).
573
574 **Discussion**
575 The discovery of taxanes and their biomimetics opened the possibility of blocking the
576 cytomotive switch in the straight microtubule (MT) conformation (21). By stabilizing MTs in this
577 state, these compounds prevent the generation of pulling forces and, consequently, the
578 segregation of sister chromatids during mitosis, while maintaining the structural integrity of the
579 microtubule network. In principle, such an approach to tubulin-targeted therapy should inhibit cell
580 division and angiogenesis without compromising the structural functions of MTs in axons.

581 Therefore, it was initially expected to cause less neurotoxicity than vinca alkaloids and other
582 microtubule-destabilizing agents (MDAs), whose mechanisms of action rely on MT
583 depolymerization (19). However, after their clinical approval in 1992, paclitaxel and other MSAs
584 targeting the paclitaxel site—docetaxel, cabazitaxel, and ixabepilone—were shown to induce
585 stronger and more persistent neurotoxic effects than vinca domain–binding drugs (23, 24). Early
586 structural studies revealed that paclitaxel-induced MT stabilization occurs at the cost of lattice
587 perturbation (33, 35), and that the addition of paclitaxel to preassembled MTs leads to changes
588 in the number of PFs (44). Given that structural features are critical for MAP recognition and
589 binding (1, 26), it is reasonable to propose that the observed neurotoxicity—and its long-lasting
590 nature—arise from altered microtubule architecture induced by these drugs.
591 Building upon our previous work (21, 25, 34), which demonstrated that nearly all drug-
592 mediated MT stabilization occurs at the expense of structural distortion, we sought to investigate
593 in depth the structural consequences of MSA-induced microtubule stabilization.
594 Microtubule structure is primarily defined by two parameters—the helical pitch and the
595 diameter—which together determine the overall lattice geometry. A third structural parameter, the
596 PF twist, cannot be resolved by fiber diffraction. The helical pitch reflects the average monomer
597 length, while the diameter is determined by the number of PFs. We observed a binary behavior
598 in the monomer length, which adopts only two distinct states: compressed (4.06 nm) or expanded
599 (4.17 nm). Compounds containing a taxane core expand the lattice from the apo (4.06 nm) to the
600 expanded (4.17 nm) state, as previously described for GMPCPP (37, 39), paclitaxel, docetaxel,
601 and related derivatives (21). The same behavior is observed for epothilones, whereas other
602 chemotypes that bind to the paclitaxel site—such as discodermolide, zampanolide, cyclostreptin,
603 and taccalonolide—or those binding to the laulimalide/peloruside site, do not induce lattice
604 expansion.
605 Together with previous results (21), these findings indicate that lattice expansion is neither
606 linked to occupancy of the taxane site nor to stabilization, as baccatin III, a non-stabilizing taxane
607 also expands the microtubule lattice. Expansion is not related to the molecular size of the ligand,
608 since both bulky (paclitaxel, docetaxel) and less bulky (epothilones, baccatin III) compounds
609 induce this effect. Moreover, the longitudinal expansion prompted by taxanes is abolished in the
610 presence of small C-7 modifications (for example, alatax), even though in this case the observed
611 compression can be reversed upon addition of GMPCPP. Interestingly, taxanes and
612 epothilones, despite their distinct interactions with Aspβ226 and Hisβ229 in H7, share a key
613 anchoring point because both chemotypes accept a hydrogen bond from the backbone nitrogen
614 of Thrβ276, located immediately before the M-loop, which is crucial for establishing lateral
615 contacts between neighboring PFs within the microtubule lattice (**Figure S1**). Nonetheless,
616 hydrogen bonding to Thrβ276 is also used by compactness-promoting ligands such as
617 zampanolide (which forms a covalent adduct with Hisβ229 in H7) and discodermolide (whose δ-
618 lactone accepts a strong hydrogen bond from Nε of Hisβ229) although these drugs also act as
619 hydrogen bond donors to this residue. On the contrary, taccalonolide AJ binds covalently to the
620 carboxylate of Aspβ226, does not hydrogen bond to Thrβ276, and does not promote expansion.

621 It is worth noting that Aspβ226 and Hisβ229 lie on one side of H7, facing the taxane site, whereas
622 Tyrβ224 and Asnβ228 face the nucleotide at the E-site on the opposite side of the helix. Therefore,
623 small changes in the orientation or straightness of H7 may be propagated between the E-site and
624 the M-loop, thereby influencing both PF compactness and lateral associations in a ligand-
625 dependent manner. Thus, H7 likely acts as a transducer that communicates structural signals
626 between the taxane-binding site and the E-site so that the nucleotide phosphates can adopt
627 alternative conformations and this, in turn, affects the β-tubulin T3 and T5 loops and the α-tubulin
628 T7–CH8 region.

629 Strikingly, although C-7-modified taxanes and laulimalide/peloruside-site ligands compact
630 the lattice, they still allow expansion in the presence of GMPCPP at the E-site of β-tubulin. In
631 stark contrast, discodermolide and zampanolide stabilize the compacted conformation even in
632 the presence of GMPCPP. This resistance to expansion likely reflects the exceptionally high
633 binding affinity of discodermolide and the covalent nature of zampanolide binding, both of which
634 override the typical expanding effect of GMPCPP probably by enforcing the conformational state
635 that is most favorable for their optimal interaction. The likely importance of the diverse interactions
636 with Thrβ276 is reinforced by the finding that dactylolide, a precursor of zampanolide that lacks
637 the specific amide side chain, produces an expanded lattice.

638 Taken together, these findings strongly suggest that the compacted and expanded lattice
639 states are energetically close, and that minimal chemical modifications can switch between them.
640 This structural plasticity provides a mechanism for transmitting chemical signals through the
641 lattice. It is also important to note that fluorescent probes can themselves alter microtubule
642 conformation, a factor that should be carefully considered when selecting probes. Among those
643 tested (**Table I**), two aniline-based probes (3´N-PT, 12.3 PF; and 2-AB-PT, 12.5 PF) stabilize the
644 expanded conformation, whereas those containing C-7-linked fluorophores (FTX1, 14.1 PF;
645 FTX2, 14.2 PF; FCH3, 14.3 PF; and HXFTX, 14.0 PF) stabilize compacted lattices.

646 Interpreting changes in mean microtubule diameter (i.e., PF number) in terms of ligand
647 chemotype is more complex. Nonetheless, compounds that induce lattice expansion typically
648 cause only moderate alterations in microtubule diameter, producing small adjustments in PF
649 number (33, 35). The maximal changes observed are a loss of up to 0.6 PFs (1.2 PFs in the case
650 of baccatin III) or a gain of 0.2 PFs. Conversely, taxane-site ligands that stabilize the compacted
651 state tend to increase the PF number by up to 1.6. Peloruside/laulimalide-site ligands stabilize
652 highly compacted microtubules with an average of 11.8 PFs (Estévez-Gallego, 2023 #3257),
653 while GMPCPP promotes expansion even in large PF-number microtubules. By combining
654 GMPCPP with different drugs, compressed microtubules can range from 11.8 PFs (peloruside A)
655 to 14.5 PFs (zampanolide), and expanded microtubules from 11.5 PFs (peloruside A and
656 paclitaxel) to 14.6 PFs (hexaflutax and GMPCPP).

657 These results illustrate how relatively subtle perturbations at the interdimer or IPF
658 interfaces induced by stabilizing ligands translate into significant, measurable differences in MT
659 compactness and PF number, as quantified by the methods described here and in previous
660 studies (25, 34, 41, 58). Our modelling studies indicate that as discussed previously (59, 60), the

661 stabilization of lateral contacts between PFs that leads to the curved-to-straight conformational
662 transition relies on a loop-mediated latch model in which Hisα283 and Tyrβ283 in the M-loops of
663 α- and β- subunits, respectively, play the role of a rotating bolt and the H1-S2/H2-S3 of the lateral
664 partner act as the stationary keepers (**Figure 11**). In the case of the β-subunit, besides the
665 hydrogen bond between O(Tyrβ283) at the minus end of the M-loop helix and NH(Argβ88) in the
666 neighboring β-tubulin subunit, our modeled complexes reveal another hydrogen bond between
667 O(Glnβ282) in the M-loop and NH(Alaβ57) in the 56–59 twisted β-hairpin of the neighboring β-
668 tubulin subunit. Conceivably, this interaction network is sensitive to the presence of a bound ligand
669 in the taxane-binding site in such a way that the spatial relation between the M-loop
670 (278RGSQQY283) in one β-tubulin subunit and the twisted β-hairpin (53YNEAAGNKYV62) of the
671 β-subunit in the neighboring PFs changes slightly but sufficiently to act as a wedge that can either
672 increase or decrease the interPF angle and thereby lead to MTs with a higher or lower number of
673 PFs. Furthermore, since helix H7 and the following T7 loop in β-tubulin link the intra- and
674 interdimer interfaces where the bound nucleotide resides, the distinct interactions of taxane-site
675 ligands with the exposed side chains of Aspβ226 and Hisβ229 in helix H7 are likely to have an
676 impact on the rate of GTP hydrolysis, as reported here for paclitaxel, epothilone A and
677 discodermolide.

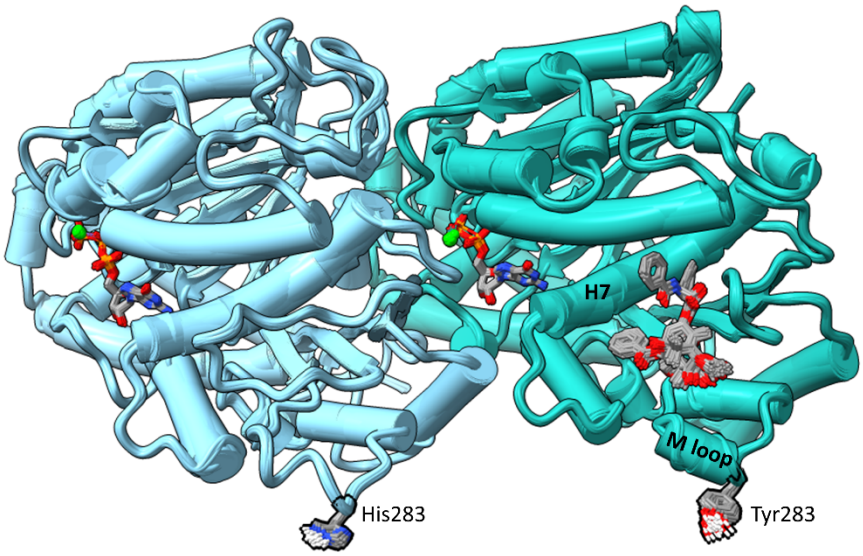

678

679 **Figure 11**. Overlay of 50 snapshots obtained from the cooling phase of the molecular dynamics
680 simulation of the β1-α2 interface in a protofilament with paclitaxel bound at the taxane site of the
681 beta subunit between helix H7 and the M-loop. The diagrammatic cylinder/stub representation
682 was obtained with ChimeraX v.1.10 and depicts the spatial relation between nucleotide- and
683 drug-binding sites. The side chains of His283 in the α-subunit and Tyr283 in the β-subunit act as
684 latches to reinforce the IPF interactions involving the H10-S2 and H2-S3 loops of tubulin
685 molecules in the neighboring PF.

686 Moreover, the results obtained for discodermolide highlight the importance of exploring
687 the three-dimensional conformational landscape of "linear" ligands in aqueous solution to assess
688 their true structural preferences and the potential for preorganization, as previously proposed to

689 explain the high antitumor potency of a linear zampanolide analogue (61). These examples
690 challenge the traditional medicinal chemistry notion that increased conformational flexibility is
691 necessarily detrimental to protein-binding affinity and biological activity.

692 The structural changes observed here underscore the remarkable plasticity of tubulin,
693 which can assemble into multiple polymeric forms (microtubules, sheets, rings, and others) by
694 accommodating distinct longitudinal and lateral contacts (27, 62). Although it was already known
695 that microtubules can modify their architecture in response to changes at the nucleotide (37, 39,
696 63), taxane (21, 44), and laulimalide/peloruside sites (25), the timescale required for structural
697 rearrangements in assembled polymers was previously unknown. Our data shows that co-
698 assembly or post-assembly drug addition produces the same final state with respect to lattice
699 expansion or compaction, whereas changes in PF number require considerably longer
700 equilibration times and do not yield perfectly identical structures (42).

701 Since ligand binding to the luminal taxane site is extremely fast (64-66), the rate-limiting
702 step for these structural transitions must be the intrinsic flexibility of the microtubule lattice. As
703 shown in **Figure 5,** the longitudinal expansion induced by compounds promoting the expanded
704 state occurs almost instantaneously—within the temporal resolution of our measurements—
705 whereas changes in PF number are comparatively slower (44), consistent with the energetic cost
706 of adding or removing PFs from an existing lattice.

707 Another long-standing question in the field concerns the stoichiometry of drug binding
708 required to alter microtubule structure. Because drug dosage varies in clinical use, the degree of
709 taxane-site occupancy may differ among treatments. Our results indicate that the structural
710 transition occurs at low saturation levels: 0.4–0.6 for paclitaxel and ixabepilone, and below 0.4 for
711 docetaxel. The transition appears to be binary, with no intermediate states detected. These
712 observations illustrate that the energetic difference between the compacted and expanded lattice
713 states is minimal and that the conformational transitions occur rapidly, consistent with their
714 proposed role as structural signals for protein-protein recognition. Environmental chemical
715 changes induced by small molecules can thus be transduced into microtubule structural
716 rearrangements, modulating their biochemical and mechanical properties. For example, we found
717 that microtubule-expanding drugs as paclitaxel and epothilone A significantly reduce the rate of
718 nucleotide hydrolysis, which could contribute to enhanced stabilization. Conversely,
719 discodermolide—because of its unique high-affinity binding mode—not only stabilizes
720 microtubules but also markedly accelerates nucleotide hydrolysis.

721 Finally, we examined how the structural determinants of MT lattices influence recognition
722 and function of two key MAPs: kinesin and tau. We found that drug binding alters kinesin motility
723 (**Figure 7**), with distinct effects depending on the lattice state—expanded or compressed—
724 induced by each ligand. Kinesin velocity is higher on expanded lattices and in the presence of
725 lower-affinity stabilizers (FB44, FB53, pelophen B), but slower on strongly stabilized compressed
726 lattices. Landing rates decrease on expanded lattices and in zampanolide-stabilized MTs, which
727 also show an increased number of PFs. Interaction times (dwell times) remain broadly similar
728 across conditions except for epothilone B, which shortens them. Run lengths are largely

729 unaffected, with the exceptions of epothilone B (decrease) and pelophen B (increase). These
730 results suggest that the tested drugs modulate kinesin–lattice interactions by reshaping the
731 energy landscape of stepping and binding: expansion combined with weaker stabilizers facilitates
732 stepping (faster motion), whereas strong compression hampers progression (slower motion).
733 Notably, epothilone B decouples velocity from binding stability—although the lattice is expanded,
734 its lower on-rate and shorter dwell time yield briefer runs despite maintained speed.

735 Regarding tau, we observed a clear preference for compressed lattices, regardless of
736 ligand chemotype, consistent with previous results from our group with taxanes (42). However,
737 marked differences arise depending on the stabilizing ligand. Tau binding is almost instantaneous
738 for MTs stabilized by zampanolide (14.5 PF, compressed), laulimalide (14.0 PF, compressed),
739 and discodermolide (12.9 PF, compressed), whereas it is significantly slower for those stabilized
740 by peloruside A (11.9 PF, compressed), pelophen B (13.0 PF, compressed), flutax-2 (13.7 PF,
741 compressed (42)), and other C-7-modified taxanes such as FB44 (13.6 PF, compressed) and
742 FB53 (12.8 PF, compressed (42)). These differences likely stem either from the distinct positions
743 of their binding sites (the taxane site lies within the MT lumen, whereas the laulimalide/peloruside
744 site is on the MT surface) or from the differential impact of the long side chain on local lattice
745 organization.

746 Conversely, tau binds expanded lattices at a much slower rate. In this study, we examined
747 two expanding chemotypes—docetaxel (13.0 PF, expanded) and epothilone B (12.7 PF,
748 expanded)—and obtained results consistent with previous data for paclitaxel (12.3 PF, expanded
749 (42)). Overall, the slowest tau binding was observed for docetaxel-stabilized MTs. These results
750 reinforce the clear preference of tau for compressed over expanded lattices, as reported
751 previously (67, 68). The observation that tau forms cohesive envelopes support that the
752 cooperative mechanism in which the lattice itself adjusts to accommodate tau's conformational
753 preferences. Nevertheless, in line with earlier studies, GMPCPP-expanded lattices are unable to
754 undergo such adaptation.

755 Analysis of the tau binding kinetics (**Figure 9**) reveals three characteristic different
756 behaviors depending on the bound drug. First, in MTs stabilized by zampanolide, laulimalide, or
757 discodermolide, tau rapidly decorates the entire filament within seconds, continuing to bind until
758 saturation. This indicates that these lattices are preorganized for tau recognition, requiring little or
759 no conformational rearrangement during binding. Second, in other compressed lattices, tau
760 envelopes form rapidly and subsequently grow, implying that these MTs can easily convert into
761 the tau-preferred conformation. Third, in lattices expanded by paclitaxel, docetaxel, or epothilone
762 B, tau binds diffusively and forms envelopes only slowly at high tau concentrations. This behavior
763 suggests that tau competes with the bound stabilizers, locally displacing them and creating
764 compacted patches that gradually expand as tau remodels the lattice. Finally, GMPCPP-stabilized
765 lattices, where the stabilizing agent is non-exchangeable, remain locked in an expansion state
766 that prevents conversion to a tau-binding conformation.

767 In this study, we have used our extensive library of MSAs to construct a comprehensive
768 structural atlas of tubulin modulation by small molecules. We demonstrate that low site occupancy

769 by distinct chemotypes allows fine-tuned control of MT architecture, enabling immediate and
770 reversible modulation of lattice conformation upon drug binding. These structural alterations
771 directly influence fundamental MT properties such as GTP hydrolysis rates and MAP interactions,
772 particularly those of kinesin and tau. This introduces a previously unrecognized layer of control,
773 positioning MSAs not only as stabilizing agents but also as molecular tools for probing and
774 manipulating MAP recognition patterns. Our findings open new avenues for precisely engineering
775 MT behavior in both mechanistic and therapeutic contexts.
776
777 **Summary**
778 Binding of stabilizing drugs to MTs alters their structure both longitudinally (through lattice
779 expansion) and laterally (by changing the number of PFs). In the longitudinal axis, only two
780 conformational states are possible: a compressed lattice (monomer rise of 4.06 nm) and an
781 expanded lattice (monomer rise of 4.17 nm). The energetic differences and transition barriers
782 between these two states are small, as even low stoichiometric ratios of a bound drug can shift
783 the equilibrium, and lattice expansion occurs within seconds after drug incorporation.
784 In contrast, multiple configurations are possible for lateral contacts, consistent with the
785 variable PF numbers observed among microtubules. Although the energetic differences between
786 MTs with different PF numbers are minor—again allowing low stoichiometric ratios of drug to
787 influence equilibrium—the energy barriers separating these states are considerably higher.
788 The conformational effects of these compounds can be finely tuned through subtle
789 chemical modifications, such as acylation of the C-7 secondary alcohol in paclitaxel. These
790 structural alterations are mirrored in the chemical properties of MTs, including their phosphatase
791 activity, and profoundly influence their recognition by tau and kinesin. Together, these findings
792 underscore the role of MT structure as a dynamic signaling platform that integrates chemical,
793 mechanical, and regulatory cues.
794
795 **Materials and Methods**
796 ***Proteins and chemicals.***
797 Purified calf brain tubulin containing a mixture of isotypes (69) was obtained as
798 described(70) and used for biochemical, and fiber diffraction experiments. Tau-mCherry was
799 expressed and purified as described previously (55). Human Kif5B-eGFP (amino acids 1–905),
800 containing a C terminal fluorescent-tag followed by a 3C protease cleavage site and a 6 × His-
801 tag was expressed and purified as in (71) with some modifications. Prior to purification, cells were
802 re-suspended in 1:1 ratio of lysis buffer (30 mM HEPES pH 7.5, 300 mM NaCl, 0.5 mM ATP, 5%
803 glycerol, 20 mM imidazole, 0.5 M TCEP) supplemented with 1× Protease inhibitor cocktail and
804 benzonase to the final concentration of 25 units/ml. Cells were homogenized by repeated
805 pipetting. Cells were lysed by spinning for 45 min at 40,000 rpm in 45 Ti fixed-angle rotor
806 (Beckman Coulter) at 4 ºC. The supernatant was incubated with pre-equilibrated HisPUR NiNTA
807 agarose resin (Thermo Fisher Scientific) for 1 h in a tightly closed gravity-flow column (Thermo
808 Fisher Scientific) at 4 ºC by slowly rotating. Subsequently, the resin was washed once lysis buffer

809 and then with buffer B (30 mM HEPES pH 7.5, 300 mM NaCl, 0.5 mM ATP, 5% glycerol, 30 mM
810 imidazole, 0.5 M TCEP). The protein was eluted from the resin after an overnight cleavage of the
811 6 × His-tag with 3C HRV protease in lysis buffer at 4 ºC. The eluted protein was further purified
812 via size-exclusion chromatography on Superdex® 200 10/300 GL column equilibrated in
813 exclusion buffer (30 mM HEPES pH 7.5, 300 mM NaCl, 0.5 mM ATP, 5% glycerol, 0.5 M TCEP).
814 Peak fractions were analyzed via SDS-PAGE, pooled and the protein was concentrated with
815 Amicon Ultra-15 Centrifugal Filter tubes (Millipore). Purified proteins were aliquoted, snap-frozen
816 in liquid N_2, and stored at –80 ºC.

817 GTP and GMPCPP were from Jena Biosciences (Jena, Germany). Sodium molybdate
818 and Malachite green oxalate were from Sigma-Aldrich. Paclitaxel was from Alfa Aesar Chemical,
819 docetaxel was kindly provided by Rhône Poulenc Rorer, Aventis (Schiltigheim, France),
820 cabazitaxel and baccatin III were from Sigma, epothilones A, B, D, taccalonolide AJ and
821 ixabepilone were from MedChemExpress; laulimalide and peloruside A were provided by Victoria
822 University of Wellington; chitax 40, 101 y 102, 2-aminopaclitaxel, 3'N-aminopaclitaxel, flutax-1,
823 flutax-2, Fchitax-3, 2-m-azido-baccatin III, hexaflutax, alatax, discodermolide, zampanolide,
824 dactylolide, TB282, cyclostreptin, pelophen B and CW235 were synthesized as described (21,
825 64, 66, 72-81). FB44 and FB53 were synthesized as described (42). GS305 was synthesized as
826 described (10.26434/chemrxiv-2024-nwb48). The synthesis and characterization of pelophen B
827 is described in patent PCT/EP2014/075903

828 All compounds were diluted in 99.8% DMSO-d_6 (Merck) to a final concentration of 20 mM
829 and stored at –70 ºC.
830

831 ***Microtubule shear-flow alignment and X-ray fiber diffraction experiments.***

832 MTs were assembled from purified bovine brain tubulin (100 mM) in PM buffer (80 mM K-
833 PIPES, 1 mM EGTA, 1 mM dithiothreitol, 0.2 mM Tris, 3 mM $MgCl_2$, pH 6.8) and either 2 mM GTP
834 or 0.5 mM GMPCPP, 2 mM GTP or 0.5 mM GMPCPP and the desired concentration of drug, (200
835 mM in the case of the static experiments), 2 mM GTP + 10 mM BeF_3^-, 2 mM GTP + 500 mM $AlCl_3$
836 + 2 mM HKF_2, 2 mM GTP + 10 mM BeF_3^- + 200 mM paclitaxel or 2 mM GTP + 500 mM $AlCl_3$ + 2
837 mM HKF_2 + 200 mM paclitaxel. Static X-ray fiber diffraction data of microtubules were collected
838 in BL11-NDC-SWEET beamline of ALBA Synchrotron, Cerdanyola del Vallès (Spain) at λ = 0.827
839 nm, as described in (34).

840 Data were processed using our in-house developed software FiDAT (Fernández et al.
841 manuscript in preparation), dimer/monomer length (from the 4th harmonic of the first layer-line
842 signals) were determined as described (25, 34) while radial structural parameters (microtubule
843 diameter, and average PF number) were determined from the position of the J_{02} maxima
844 according to J_{02} = 1.045/R assuming an IPF mean distance of 5.7 nm (35).

845 Kinetic X-ray fiber diffraction experiments were performed at BL40XU beam line of
846 Spring-8, Hyogo, Japan. An aliquot of 100 µL of the suspension containing the assembled MTs at

847 a 100 μM concentration was collected and applied onto the shear-flow apparatus. The top end of
848 the apparatus was opened to enable free access to the specimen, where we set an electric pipette
849 (eLine, Sartorius, Gettingen, Germnay) directly connected to a wireless shutter controller
850 (Oppilas/L1, Pixel, China). At t = 40 s, 1 μL of DMSO stock solution containing 20 mM of stabilizers
851 (paclitaxel, docetaxel, chitax 40, baccatin III and laulimalide) was added by remote control of the
852 electric pipette to the solution to reach a final concentration 100 μM. Diffraction signals were
853 measured employing a 0.8 m camera length and exposure of 0.95 s and a Pilatus 200K, 475 ×
854 195 pixels (Rigaku, Tokyo, Japan) detector using ImageJ, ver. 1.53c (NIH, USA). The average
855 monomer length of the tubulin monomer was estimated from the 1 nm^{-1} layer line. Calibration of
856 the spacing of diffraction reflections was performed using a standard 4.97 nm signal in powder
857 diffraction using lead stearate. One pixel in the detector corresponded to the spatial frequency in
858 a reciprocal space of 0.0011 nm^{-1}. The peak position was determined by fitting each of the
859 obtained signal profiles to a Lorentzian function.
860
861 ***In silico model building and molecular dynamics simulations.***

862 *Ab initio* geometry optimization and derivation of atom-centered RESP charges (82) for
863 docetaxel, epothilone A, zampanolide, discodermolide and alatax were accomplished by using
864 the density functional tight-binding method, a 6-31G(d,p) basis set, and the IEF-SCRF continuum
865 solvent model (83)) for water, as implemented in program Gaussian 09 (Revision D.01) (84). This
866 procedure has been reported earlier for other tubulin ligands (85) and for the covalent adducts of
867 taccalonolide AJ and zampanolide with Aspβ226 and Hisβ229, respectively (45). Bonded and
868 non-bonded parameters for these taxanes were obtained from the general AMBER force field
869 *gaff2* (86). The conformational preferences of discodermolide in explicit water were studied upon
870 immersion of this ligand (as found in PDB entry 6SES) in a cubic box of TIP3P water molecules
871 and simulation at 300 K for 300 ns using molecular dynamics (MD) followed by simulating
872 annealing and energy minimization, as performed earlier for other drugs (42, 87).

873 For the ligand-bound macromolecular assemblies representing three parallel short PFs,
874 each consisting of two concatenated head-to-tail dimers (i.e., (α1:β1-α2:β2)/(α1':β1'-
875 α2':β2')/(α1":β1"-α2":β2")), use was made of PDB entries 6DPU and 6DPV (88), which depict a
876 stretch of an expanded or compacted 14-PF MT, respectively, and PDB entry 3JAK (89), which
877 corresponds to a symmetrized reconstruction of a compacted 13-PF MT. Missing residues 38–46
878 in each α subunit were grafted from AlphaFold model AF-P81947-F1-v4 for completeness.
879 Residue numbering and secondary structure assignment herein follow the α-tubulin-based
880 definitions (90), as is customary in the Protein Data Bank.

881 The refined 6DPV and 3JAK MT patches were used as input to the elNémo web server
882 (91) to build the corresponding anisotropic elastic network models (ENM) (92) and carry out the
883 normal mode analyses (NMA) employing the default values for cutoff (12 Å), force constant (1.0
884 kcal mol^{-1} $Å^{-2}$) and maximum displacement (amplitude <2 Å).

885 The interdimer space was first explored in a series of minimalist (b1:a2) complexes
886 originating from PDB entries 6DPU (expanded) and 6DPV (compacted) in which all Ca atoms -
887 except those in the more flexible and less well-defined loop regions- were positionally restrained
888 by means of a weak harmonic force constant (2.0 kcal mol^{-1} $Å^{-2}$) to preserve the gross
889 characteristics of each MT subtype. The GTP molecule in the N-site of α-tubulin and either GTP
890 or GDP in the E-site of β-tubulin, together with their partially hydrated coordinated Mg^{2+} ions, were
891 initially located as reported in the high-resolution X-ray crystal structures deposited with PDB
892 codes 4I4T and 8BDE. These systems were firstly energy refined and then simulated at 300 K for
893 100 ps using the *ff14SB* force field (93) for protein atoms, the TIP3P model for the few explicit
894 water molecules, and the generalized Born model for the bulk solvent (94), as implemented in the
895 *pmemd.cuda_SPFP* engine of AMBER 18. The resulting equilibrated systems were then
896 subjected to a simulated annealing procedure by gradually decreasing the temperature from 300
897 K to 100 K over a period of 150 ps.

898 The different (α1:β1-α2:β2)/(α1':β1'-α2':β2')/(α1":β1"-α2":β2") complexes in the apo and
899 holo states were then simulated under the same conditions for 200 ps. alatax and docetaxel were
900 best-fit superimposed onto the structure of bound paclitaxel, as reported earlier for similar
901 molecules (21). Discodermolide and epothilone B were docked in the β subunits so as to
902 reproduce the binding poses found in PDB entries 6SES and 7DAE, respectively. Construction of
903 the covalent adducts with taccalonolide AJ and zampanolide followed a previously reported
904 procedure (45). By following this procedure, six replicas of each bound ligand and ligand-binding
905 site were sampled simultaneously. The resulting equilibrated MT patches were cooled down from
906 300 K to 100 K over 400 ps and then energy minimized in the absence of any restraints. Next,
907 each refined 3´2-patch of tubulin dimers was replicated six times in PyMOL, as recently described
908 for similar systems (42), and the (α1:β1-α2:β2-α3:β3) stretch of the first copy was best-fit
909 superimposed onto the (α1":β1"-α2":β2"-α3":β3") stretch of the optimized model. Thereafter, the
910 (α1:β1-α2:β2-α3:β3) stretch of each remaining copy was best-fit superimposed onto the (α1":β1"-
911 α2":β2"-α3":β3") stretch of the preceding model. This process led quite naturally to the formation
912 of a tubular structure consisting of 13 or 14 straight PFs (**Figure S2**) with one drug molecule
913 bound in the taxane site of every β subunit. Lastly, the macromolecular ensemble was cleaned
914 up by removing the redundant overlaid copies to produce an all-atom model of the MT lattice,
915 which was subjected to a final energy refinement and sequential chain renumbering. For the 12-
916 and 15-PF MTs, each (α1:β1-α2:β2-α3:β3) copy was best-fit superimposed onto the
917 corresponding PF stretch of the harmonically deformed model obtained from the NMA (**Supp.
918 Movie 11**).

919 The resulting MT pieces representative of a full turn of laterally associated PFs with bound
920 paclitaxel, docetaxel, epothilone B, discodermolide, zampanolide and taccalonolide AJ have been
921 deposited in the publicly available ModelArchive (www.modelarchive.org) database with
922 accession codes ma-rkctk, ma-x9q02, ma-2embb, ma-ir5i7, ma-qcuyh, and ma-qzvr1,
923 respectively. The atomic model of a MT piece containing bound alatax can be inferred from that
924 bound to Flutax-2 (ma-ayvpr) (42). The first non-trivial normal mode calculated for the Ca trace

925 of the refined paclitaxel-bound 12-PF MT clearly shows the closing motion that leads to
926 heterotypic seam sealing (**Supp. Movie 11).**
927
928 ***Measurement of nucleotide hydrolysis.***

929 Nucleotide hydrolysis by MTs was in MEDTA (100 mM potassium 2-(*N*-
930 morpholino)ethanesulfonic acid (K-MES), 1 mM EDTA, 3.4 M glycerol, pH 6.7) buffer containing
931 6 mM $MgCl_2$ and 1mM GTP. Firstly, 10 mg of lyophilized tubulin was re-suspended in 0.5 mL
932 MEDTA buffer, containing 0.1 mM GTP or 0.001 mM GMPCPP and without $MgCl_2$. The protein
933 solution was subjected to size-exclusion chromatography with a column of Sephadex G-25
934 medium (30 × 0.9 cm) to remove the trehalose and phosphate present in the storage buffer. Next,
935 aggregates were removed by centrifuging at 50.000 rpm for 10 minutes at 4 °C using a Beckman
936 Optima MA-XP ultracentrifuge (Beckman Coulter) equipped with a TLA 120.2 fixed-angle rotor
937 (Beckman-Coulter). Tubulin concentration was determined by absorption spectrophotometry
938 using a UV-vis spectrophotometer (Evolution 201 spectrophotometer, Thermo Scientific) with 1
939 cm light path quartz cuvettes. Absorbance spectra, ranging from 240–340 nm, were recorded
940 after preparing a 1/20 dilution with NaPi-SDS buffer. The concentration of tubulin was calculated
941 using the molar extinction coefficient (ε) of 107000 M^{-1} cm^{-1} at λ = 275 nm as mentioned above.
942 After calculating the concentration of tubulin, 6 mM $MgCl_2$ and 0.9 mM GTP or 0.099 mM
943 GMPCPP (to obtain a final concentration of 1 mM GTP or 0.1 mM GMPCPP) were added to the
944 sample.

945 Tubulin polymerization was induced by raising temperature to 37ºC (polymerization was
946 followed at λ = 355 nm in an Appliskan® plate reader (Thermo Scientific) and the phosphate
947 released was measured using the malachite green inorganic phosphate assay (49). Briefly, a 20
948 µL aliquot of the polymerized solution was diluted with 280 µL of milli-Q water and 300 µL of
949 malachite green solution (0.2% sodium molybdate, 0.03% malachite green oxalate, 0.05% Triton
950 X-100, 0.7 M hydrochloric acid) was added, mixed thoroughly, and incubated. Absorbance was
951 measured at λ = 650 nm and phosphate concentrations in the samples were calculated by
952 comparison with sodium phosphate standards. Nucleotide content in drugged assembled MTs
953 was quantified by centrifugation and HPLC as described in (95).
954
955 ***In vitro tau and kinesin- drug stabilized microtubules binding assay.***
956 The *in vitro* binding of Kif5B1-950-eGFP and tau441-mCherry to drug stabilized MTs was
957 measured using TIRF microscopy as described in (96) by replacing paclitaxel with the desired
958 drug. TIRF microscopy experiments were performed on an inverted widefield microscope
959 Nikon-Ti2 E, equipped with a motorised XY-stage, a perfect focus system, Apo TIRF 60× oil NA
960 1.49 objective and PRIME BSY (Teledyne Photometrics) camera. MTs were visualized using
961 Interference Reflection microscopy (IRM) and fluorescently labelled proteins were visualized
962 sequentially by switching between microscope filter cubes for GFP and mCherry channels. The

963 microscope was controlled using NIS Elements software (Nikon). All experiments were conducted
964 at RT.
965 Microscopy chambers were prepared from two sandwiched silanized glass coverslips (22
966 × 22 mm and 18 × 18 mm) attached through parafilm strips (heated for 15–20 s at 60 °C and
967 gently pressed together) to form ~2.5 mm wide parallel flow channels. Prior to the chamber
968 assembly, the coverslips were washed in 3 M KOH, cleaned using Zepto plasma cleaner (Diener
969 electronic) and silanized with hexamethyldisilazane. Flow channels were first incubated with 40
970 µg mL^{-1} anti-biotin antibodies (Sigma, B3640) in PBS for 10 min, followed by incubation with 1%
971 Pluronic F127 (Sigma Aldrich, P2443) in PBS for at least 1 hour. Then, F127 was washed with
972 BRB80 (80 mM PIPES, 1 mM EGTA, 1 mM $MgCl_2$, pH 6.9).
973 The MTs employed were assembled from porcine brain tubulin isolated using the
974 high-molarity PIPES procedure (97). MTs were assembled using 2% biotin-labelled tubulin
975 (Cytoskeleton Inc., T333P). Drug-stabilized, pre-assembled MTs (polymerized, stored and
976 imaged in presence of desired drug) were polymerized from 4 mg mL^{-1} 2%-biotinylated tubulin
977 for 30 min at 37 °C in BRB80 supplemented with 4 mM $MgCl_2$, 40 µM of the desired drug using
978 5% DMSO, and 1 mM GTP (Jena Bioscience, NU-1012). MTs were centrifuged for 30 min at
979 18,000×*g* in a Microfuge 18 Centrifuge (Beckman Coulter). The pellet was re-suspended and kept
980 in BRB80 supplemented with 10 µM of the desired drug. GMPCPP stabilized MTs (GMPCPP
981 polymerized) were assembled from 4 mg mL^{-1} 2% biotinylated tubulin for 2 h at 37 °C in BRB80
982 supplemented with 1 mM $MgCl_2$ and 1mM GMPCPP (Jena Bioscience, NU-405). Polymerized
983 MTs were centrifuged for 30 min at 18,000x*g* in a Microfuge 18 Centrifuge (Beckman Coulter)
984 and pellets were re-suspended and kept in BRB80.
985 Stabilized MTs were flushed into the channel and incubated for 10–20 seconds to allow
986 for surface attachment. Unbound MTs were removed by washing with BRB80 supplemented with
987 10 µM of the desired drug. Prior the experiment, the solution was exchanged by motility buffer
988 (BRB80 containing 10 mM DTT, 20 mM D-glucose, 0.1% Tween-20, 0.5 mg/mL casein, 1 mM
989 Mg-ATP, 0.02 mg/mL catalase, 0.22 mg/mL glucose oxidase, 10 µM drug). Subsequently, a
990 solution containing either 10.8 nM Kif5B-eGFP or 5/10/40 nM tau-mCherry in MB was introduced
991 into the chamber.
992 To assess Kif5B-eGFP motility along MTs, an IRM image (50 ms exposure) was acquired
993 followed by a 1 min video using 488 nm laser excitation (20% laser intensity, 300 ms exposure)
994 with no delay. Three to four videos were recorded from different fields within the same channel
995 and at least 2 channels were measured for each experimental condition. The same experiment
996 was done in 2 to 3 different days giving an n between 12 and 24.
997 To monitor tau-mCherry binding to MTs, 4 min videos were acquired every 7 sec. Two
998 imaging channels were recorded simultaneously, alternating between IRM (50 ms exposure) and
999 561 nm field (30% intensity, 200 ms exposure). Depending on the drug used, firstly 5/10 nM
1000 tau-mCherry was injected immediately after the first frame was acquired. Similarly, a second/third
1001 video of the same area was recorded adding an additional 10 and 40 nM tau-mCherry.
1002

Image analysis.

For representative figures, all data were collected from at least two independent trials. Unless otherwise stated, all data were analysed manually using Fiji (ImageJ) (98); graphs and statistical analyses were created and performed using GraphPad Prism v.8.0.1. Graphs represent mean data, and the error bars represent the standard errors of the mean (SEM).

Background fluorescence was subtracted from all intensity measurements. For each condition, analyses were performed on 12 randomly selected, in-focus MTs per channel, being identified with IRM.

For kinesin motility analysis, MTs were selected in the IRM channel by drawing segmented lines of 5 pixels in width. Kymographs were generated using the *KymographBuilder* plugin of Fiji. Individual motor traces were manually selected as straight lines (1 pixel thick) on the kymographs. From these traces, run length (x-axis), interaction time (y-axis), and velocity (calculated as the ratio of both) were determined using the Multiple Velocity Measurement Tool macro that applies to all ROIs in the ROI Manager of Fiji. Finally, landing rate was assessed by quantifying the number of kinesins bound along each MT and normalizing this value to the total MT length (expressed in mm) and time.

To quantify the fraction of the MT surface covered by tau envelopes, a segmented line with a fixed width of 5 px (0.36 mm) was manually traced along either the envelope-covered regions or the full length of individual MTs. The total length of all envelope segments was then divided by the corresponding MT length to yield the percentage of coverage. This analysis was conducted at multiple time frames: four time points (12 s, 1, 2 and 4 min) in the first video recorded under 5/10 nM tau-mCherry, and three time points (12 s, 2 and 4 min) for the subsequent conditions. To compare the amount of tau bound per micron of MT across different structural conditions, a segmented line (5 px wide) was drawn along the entire length of each MT. The integrated fluorescence intensity (IntDen) was measured, and this value was normalized to the background and divided by the corresponding MT length (in mm). This analysis was performed at three time points (12 s, 2 and 4 min) in the sequential videos.

Acknowledgements.

This work was supported by Ministerio de Ciencia e Innovación (MICIN) and FEDER, PID2022−136765OB-I00 to J.F.D. and PID2021−123399OB-I00 to M.A.O, by the European Molecular Biology Organization (EMBO) [short-term fellowship 11234] to R.P.O and MOSBRI (TNA) under project number MOSBRI-2024-296 to RPO. We thank staff of beamline BL-11-NCD-SWEET (ALBA, Cerdanyola del Vallès, Spain) for their support. The kinetic experiments were performed with the approval of the SPring-8 Proposal Review Committee (2016B1182, 2020A1332, 2021A1430). We also thank Ganadería Fernando Díaz for calf brains supply.

1043 ***References.***

1044 1. I. Grigoriev, A. Akhmanova, Microtubule dynamics at the cell cortex probed by TIRF
1045 microscopy. *Methods Cell Biol* **97**, 91-109 (2010).
1046 2. J. M. Wagstaff *et al.*, Diverse cytomotive actins and tubulins share a polymerization switch
1047 mechanism conferring robust dynamics. *Science Advances* **9**, eadf3021 (2023).
1048 3. R. B. Ravelli *et al.*, Insight into Tubulin Regulation from a Complex with Colchicine and a
1049 Stathmin-like Domain. *Nature* **428**, 198-202 (2004).
1050 4. R. M. Buey, J. F. Díaz, J. M. Andreu, The Nucleotide Switch of Tubulin and Microtubule
1051 Assembly: a Polymerization-driven Structural Change. *Biochemistry* **45**, 5933-5938 (2006).
1052 5. L. M. Rice, E. A. Montabana, D. A. Agard, The lattice as allosteric effector: structural
1053 studies of alphabeta- and gamma-tubulin clarify the role of GTP in microtubule assembly. *Proc*
1054 *Natl Acad Sci U S A* **105**, 5378-5383 (2008).
1055 6. S. Y. Saito, Toxins affecting actin filaments and microtubules. *Prog Mol Subcell Biol* **46**,
1056 187-219 (2009).
1057 7. M. O. Steinmetz, A. E. Prota, Microtubule-Targeting Agents: Strategies To Hijack the
1058 Cytoskeleton. *Trends Cell Biol* **28**, 776-792 (2018).
1059 8. S. Matthew *et al.*, Gatorbulin-1, a distinct cyclodepsipeptide chemotype, targets a seventh
1060 tubulin pharmacological site. *Proceedings of the National Academy of Sciences* **118**,
1061 e2021847118 (2021).
1062 9. T. Mühlethaler *et al.*, Rational Design of a Novel Tubulin Inhibitor with a Unique
1063 Mechanism of Action. *Angew Chem Int Ed Engl* **61**, e202204052 (2022).
1064 10. W. Wall, *The Search for Human Chromosomes* (2016), 10.1007/978-3-319-26336-6.
1065 11. J. Messaritakis *et al.*, High mebendazole doses in pulmonary and hepatic hydatid
1066 disease. *Archives of Disease in Childhood* **66**, 532-533 (1991).
1067 12. W. D. Sohier Jr, R. K. L. Wong, A. C. Aisenberg, Vinblastine in the treatment of advanced
1068 Hodgkin's disease. *Cancer* **22**, 467-472 (1968).
1069 13. S. M. Kupchan *et al.*, Maytansine, a novel antileukemic ansa macrolide from Maytenus
1070 ovatus. *J Am Chem Soc* **94**, 1354-1356 (1972).
1071 14. T. Usui *et al.*, The anticancer natural product pironetin selectively targets Lys352 of alpha-
1072 tubulin. *Chem Biol* **11**, 799-806 (2004).
1073 15. B. Gigant *et al.*, Structural basis for the regulation of tubulin by vinblastine. *Nature* **435**,
1074 519-522 (2005).
1075 16. A. E. Prota *et al.*, A new tubulin-binding site and pharmacophore for microtubule-
1076 destabilizing anticancer drugs. *Proc Natl Acad Sci U S A* **111**, 13817-13821 (2014).
1077 17. A. E. Prota *et al.*, Pironetin Binds Covalently to alphaCys316 and Perturbs a Major Loop
1078 and Helix of alpha-Tubulin to Inhibit Microtubule Formation. *J Mol Biol* **428**, 2981-2988 (2016).
1079 18. J. Yang *et al.*, Pironetin reacts covalently with cysteine-316 of alpha-tubulin to destabilize
1080 microtubule. *Nat Commun* **7**, 12103 (2016).
1081 19. G.-z. Li *et al.*, Vincristine-induced peripheral neuropathy: A mini-review. *NeuroToxicology*
1082 **81**, 161-171 (2020).

1083 20. R. C. Donehower, The Clinical Development of Paclitaxel: A Successful Collaboration of
1084 Academia, Industry and the National Cancer Institute. *The Oncologist* **1**, 240-243 (1996).
1085 21. A. E. Prota *et al.*, Structural insight into the stabilization of microtubules by taxanes. *eLife*
1086 **12**, e84791 (2023).
1087 22. A. E. Prota *et al.*, Structural basis of microtubule stabilization by laulimalide and
1088 peloruside A. *Angew Chem Int Ed Engl* **53**, 1621-1625 (2014).
1089 23. B. M. Cook *et al.*, Differential Morphological and Biochemical Recovery from
1090 Chemotherapy-Induced Peripheral Neuropathy Following Paclitaxel, Ixabepilone, or Eribulin
1091 Treatment in Mouse Sciatic Nerves. *Neurotox Res* **34**, 677-692 (2018).
1092 24. C. Pellacani, G. Eleftheriou, Neurotoxicity of antineoplastic drugs: Mechanisms,
1093 susceptibility, and neuroprotective strategies. *Advances in Medical Sciences* **65**, 265-285 (2020).
1094 25. J. Estévez-Gallego *et al.*, Chemical modulation of microtubule structure through the
1095 laulimalide/peloruside site. *Structure* **31**, 88-99.e85 (2023).
1096 26. A. Akhmanova, M. O. Steinmetz, Microtubule +TIPs at a glance. *J Cell Sci* **123**, 3415-
1097 3419 (2010).
1098 27. Y.-M. Chew, R. A. Cross, Structural switching of tubulin in the microtubule lattice.
1099 *Biochemical Society Transactions* **53**, 161-171 (2025).
1100 28. A. Kumar *et al.*, Short Linear Sequence Motif LxxPTPh Targets Diverse Proteins to
1101 Growing Microtubule Ends. *Structure* **25**, 924-932 e924 (2017).
1102 29. D. R. Peet, N. J. Burroughs, R. A. Cross, Kinesin expands and stabilizes the GDP-
1103 microtubule lattice. *Nature Nanotechnology* **13**, 386-391 (2018).
1104 30. V. Siahaan *et al.*, Microtubule lattice spacing governs cohesive envelope formation of tau
1105 family proteins. *Nature Chemical Biology* **18**, 1224-1235 (2022).
1106 31. T. Shima *et al.*, Kinesin-binding-triggered conformation switching of microtubules
1107 contributes to polarized transport. *J Cell Biol* **217**, 4164-4183 (2018).
1108 32. E. Gornstein, T. L. Schwarz, The paradox of paclitaxel neurotoxicity: Mechanisms and
1109 unanswered questions. *Neuropharmacology* **76 Pt A**, 175-183 (2014).
1110 33. J. M. Andreu *et al.*, Low resolution structure of microtubules in solution. Synchrotron X-
1111 ray scattering and electron microscopy of taxol-induced microtubules assembled from purified
1112 tubulin in comparison with glycerol and MAP-induced microtubules. *J Mol Biol* **226**, 169-184
1113 (1992).
1114 34. J. Estevez-Gallego *et al.*, Structural model for differential cap maturation at growing
1115 microtubule ends. *Elife* **9** (2020).
1116 35. J. M. Andreu *et al.*, Solution structure of Taxotere-induced microtubules to 3-nm
1117 resolution. The change in protofilament number is linked to the binding of the taxol side chain. *J*
1118 *Biol Chem* **269**, 31785-31792 (1994).
1119 36. R. Matesanz *et al.*, Modulation of microtubule interprotofilament interactions by modified
1120 taxanes. *Biophys J* **101**, 2970-2980 (2011).
1121 37. M. R. Mejillano, J. S. Barton, J. P. Nath, R. H. Himes, GTP analogues interact with the
1122 tubulin exchangeable site during assembly and upon binding. *Biochemistry* **29**, 1208-1216 (1990).

38. A. A. Hyman, D. Chrétien, I. Arnal, R. H. Wade, Structural changes accompanying GTP hydrolysis in microtubules: information from a slowly hydrolyzable analogue guanylyl-(alpha,beta)-methylene-diphosphonate. *Journal of Cell Biology* **128**, 117-125 (1995).

39. Gregory M. Alushin *et al.*, High-Resolution Microtubule Structures Reveal the Structural Transitions in αβ-Tubulin upon GTP Hydrolysis. *Cell* **157**, 1117-1129 (2014).

40. B. J. LaFrance *et al.*, Structural transitions in the GTP cap visualized by cryo-electron microscopy of catalytically inactive microtubules. *Proceedings of the National Academy of Sciences* **119**, e2114994119 (2022).

41. T. Sugiyama *et al.*, Quick shear-flow alignment of biological filaments for X-ray fiber diffraction facilitated by methylcellulose. *Biophys J* **97**, 3132-3138 (2009).

42. F. Bonato *et al.*, Probing the structural signaling of microtubules with engineered, chemically controlled filaments. *Nature Chem. Biol.* **Submitted** (2025).

43. E. H. Kellogg *et al.*, Insights into the Distinct Mechanisms of Action of Taxane and Non-Taxane Microtubule Stabilizers from Cryo-EM Structures. *J Mol Biol* **429**, 633-646 (2017).

44. J. F. Díaz, J. M. Valpuesta, P. Chacón, G. Diakun, J. M. Andreu, Changes in microtubule protofilament number induced by Taxol binding to an easily accessible site. Internal microtubule dynamics. *J Biol Chem* **273**, 33803-33810 (1998).

45. P. A. Sánchez-Murcia, A. Mills, Á. Cortés-Cabrera, F. Gago, Unravelling the covalent binding of zampanolide and taccalonolide AJ to a minimalist representation of a human microtubule. *Journal of computer-aided molecular design* **33**, 627-644 (2019).

46. G. Tauriello *et al.*, ModelArchive: A Deposition Database for Computational Macromolecular Structural Models. *Journal of Molecular Biology* **437**, 168996 (2025).

47. R. Ayukawa *et al.*, GTP-dependent formation of straight tubulin oligomers leads to microtubule nucleation. *J Cell Biol* **220** (2021).

48. E. Nogales, K. H. Downing, L. A. Amos, J. Lowe, Tubulin and FtsZ form a distinct family of GTPases. *Nat Struct Biol* **5**, 451-458 (1998).

49. S. G. Carter, D. W. Karl, Inorganic phosphate assay with malachite green: An improvement and evaluation. *Journal of Biochemical and Biophysical Methods* **7**, 7-13 (1982).

50. M. Paydar, B. H. Kwok, Evidence for conformational change-induced hydrolysis of β-tubulin-GTP. *bioRxiv* 10.1101/2020.09.08.288019, 2020.2009.2008.288019 (2020).

51. B. Ram Prasad, N. V. Plotnikov, J. Lameira, A. Warshel, Quantitative exploration of the molecular origin of the activation of GTPase. *Proceedings of the National Academy of Sciences* **110**, 20509-20514 (2013).

52. R. M. Buey *et al.*, Microtubule interactions with chemically diverse stabilizing agents: Thermodynamics of binding to the paclitaxel site predicts cytotoxicity. *Chem. Biol.* **12**, 1269-1279 (2005).

53. A. Canales *et al.*, Molecular recognition of epothilones by microtubules and tubulin dimers revealed by biochemical and NMR approaches. *ACS Chem Biol* **9**, 1033-1043 (2014).

54. K. J. Verhey, J. W. Hammond, Traffic control: regulation of kinesin motors. *Nature reviews. Molecular cell biology* **10**, 765-777 (2009).

1163 55. M. Genova *et al.*, Tubulin polyglutamylation differentially regulates microtubule-
1164 interacting proteins. *Embo j* **42**, e112101 (2023).
1165 56. R. Brandt, N. I. Trushina, L. Bakota, Much More Than a Cytoskeletal Protein:
1166 Physiological and Pathological Functions of the Non-microtubule Binding Region of Tau. *Front*
1167 *Neurol* **11**, 590059 (2020).
1168 57. R. Tan *et al.*, Microtubules gate tau condensation to spatially regulate microtubule
1169 functions. *Nat Cell Biol* **21**, 1078-1085 (2019).
1170 58. S. Kamimura, Y. Fujita, Y. Wada, T. Yagi, H. Iwamoto, X-ray fiber diffraction analysis
1171 shows dynamic changes in axial tubulin repeats in native microtubules depending on paclitaxel
1172 content, temperature and GTP-hydrolysis. *Cytoskeleton* **73**, 131-144 (2016).
1173 59. H. Sui, K. H. Downing, Structural Basis of Interprotofilament Interaction and Lateral
1174 Deformation of Microtubules. *Structure* **18**, 1022-1031 (2010).
1175 60. M. Á. Oliva, F. Gago, S. Kamimura, J. F. Díaz, Alternative Approaches to Understand
1176 Microtubule Cap Morphology and Function. *ACS Omega* 10.1021/acsomega.2c06926 (2023).
1177 61. C. A. Umaña *et al.*, Linear (−)-Zampanolide: Flexibility in Conformation–Activity
1178 Relationships. *ChemMedChem* **18**, e202300292 (2023).
1179 62. F. M. Ranaivoson, B. Gigant, S. Berritt, M. Joullie, M. Knossow, Structural plasticity of
1180 tubulin assembly probed by vinca-domain ligands. *Acta Crystallogr D Biol Crystallogr* **68**, 927-
1181 934 (2012).
1182 63. J. Estévez-Gallego *et al.*, Hydrolysis-deficient mosaic microtubules as faithful mimics of
1183 the GTP cap. *Nature Communications* **16**, 2396 (2025).
1184 64. J. F. Diaz, R. Strobe, Y. Engelborghs, A. A. Souto, J. M. Andreu, Molecular recognition
1185 of taxol by microtubules. Kinetics and thermodynamics of binding of fluorescent taxol derivatives
1186 to an exposed site. *J Biol Chem* **275**, 26265-26276 (2000).
1187 65. J. F. Diaz, I. Barasoain, J. M. Andreu, Fast kinetics of Taxol binding to microtubules.
1188 Effects of solution variables and microtubule-associated proteins. *J Biol Chem* **278**, 8407-8419
1189 (2003).
1190 66. J. F. Diaz, I. Barasoain, A. A. Souto, F. Amat-Guerri, J. M. Andreu, Macromolecular
1191 accessibility of fluorescent taxoids bound at a paclitaxel binding site in the microtubule surface. *J*
1192 *Biol Chem* **280**, 3928-3937 (2005).
1193 67. B. T. Castle, K. M. McKibben, E. Rhoades, D. J. Odde, Tau Avoids the GTP Cap at
1194 Growing Microtubule Plus-Ends. *iScience* **23**, 101782 (2020).
1195 68. N. Bagdadi *et al.*, Stable GDP-tubulin islands rescue dynamic microtubules. *Journal of*
1196 *Cell Biology* **223**, e202307074 (2024).
1197 69. R. F. Ludueña, A. Banerjee, "The Isotypes of Tubulin" in The Role of Microtubules in Cell
1198 Biology, Neurobiology, and Oncology, T. Fojo, Ed. (Humana Press, Totowa, NJ, 2008),
1199 10.1007/978-1-59745-336-3_6, pp. 123-175.
1200 70. J. M. Andreu, "Large Scale Purification of Brain Tubulin With the Modified Weisenberg
1201 Procedure" in Microtubule Protocols, J. Zhou, Ed. (Humana Press, Totowa, NJ, 2007),
1202 10.1007/978-1-59745-442-1_2, pp. 17-28.

1203 71. V. Henrichs *et al.*, Mitochondria-adaptor TRAK1 promotes kinesin-1 driven transport in
1204 crowded environments. *Nature Communications* **11**, 3123 (2020).
1205 72. A. A. Souto *et al.*, New fluorescent water-soluble taxol derivatives. *Angew Chem Int Ed*
1206 *Engl* **34**, 2710-2712 (1995).
1207 73. Y. Li, R. Edsall, Jr., P. G. Jagtap, D. G. Kingston, S. Bane, Equilibrium studies of a
1208 fluorescent paclitaxel derivative binding to microtubules. *Biochemistry* **39**, 616-623 (2000).
1209 74. L. He *et al.*, A common pharmacophore for Taxol and the epothilones based on the
1210 biological activity of a taxane molecule lacking a C-13 side chain. *Biochemistry* **39**, 3972-3978
1211 (2000).
1212 75. C. D. Vanderwal, D. A. Vosburg, S. Weiler, E. J. Sorensen, An enantioselective synthesis
1213 of FR182877 provides a chemical rationalization of its structure and affords multigram quantities
1214 of its direct precursor. *J Am Chem Soc* **125**, 5393-5407 (2003).
1215 76. I. Paterson, I. Lyothier, Total synthesis of (+)-discodermolide: an improved endgame
1216 exploiting a Still-Gennari-type olefination with a C1-C8 beta-ketophosphonate fragment. *Org Lett*
1217 **6**, 4933-4936 (2004).
1218 77. R. Matesanz *et al.*, Optimization of taxane binding to microtubules. Binding affinity
1219 decomposition and incremental construction of a high-affinity analogue of paclitaxel. *Chem Biol*
1220 **15**, 573-585 (2008).
1221 78. X. Li, I. Barasoain, R. Matesanz, J. F. Diaz, W. S. Fang, Synthesis and biological activities
1222 of high affinity taxane-based fluorescent probes. *Bioorg Med Chem Lett* **19**, 751-754 (2009).
1223 79. D. Zurwerra *et al.*, Total Synthesis of (−)-Zampanolide and Structure–Activity
1224 Relationship Studies on (−)-Dactylolide Derivatives. *Chemistry – A European Journal* **18**, 16868-
1225 16883 (2012).
1226 80. C. W. Wullschleger, J. Gertsch, K.-H. Altmann, Synthesis and Biological Activity of 7,8,9-
1227 Trideoxy- and 7R DesTHP-Peloruside A. *Chemistry – A European Journal* **19**, 13105-13111
1228 (2013).
1229 81. T. M. Brütsch *et al.*, Synthesis and Structure-Activity Relationship Studies of C(13)-
1230 Desmethylene-(−)-Zampanolide Analogs. *Chemistry – A European Journal* **29**, e202300703
1231 (2023).
1232 82. J. Wang, P. Cieplak, P. A. Kollman, How well does a restrained electrostatic potential
1233 (RESP) model perform in calculating conformational energies of organic and biological
1234 molecules? *Journal of Computational Chemistry* **21**, 1049-1074 (2000).
1235 83. G. Scalmani, M. J. Frisch, Continuous surface charge polarizable continuum models of
1236 solvation. I. General formalism. *J Chem Phys* **132**, 114110 (2010).
1237 84. M. J. Frisch *et al.* (2009) Gaussian 09. (Gaussian, Inc., Wallingford, CT, USA).
1238 85. Y. Ma *et al.*, Modulation of taxane binding to tubulin curved and straight conformations by
1239 systematic 3′N modification provides for improved microtubule binding, persistent cytotoxicity and
1240 in vivo potency. *European Journal of Medicinal Chemistry* **259**, 115668 (2023).
1241 86. X. He, V. H. Man, W. Yang, T. S. Lee, J. Wang, A fast and high-quality charge model for
1242 the next generation general AMBER force field. *J Chem Phys* **153**, 114502 (2020).

87. C. Coderch *et al.*, A structure-based design of new C2- and C13-substituted taxanes: tubulin binding affinities and extended quantitative structure-activity relationships using comparative binding energy (COMBINE) analysis. *Org Biomol Chem* **11**, 3046-3056 (2013).
88. R. Zhang, B. LaFrance, E. Nogales, Separating the effects of nucleotide and EB binding on microtubule structure. *Proc. Natl. Acad. Sci. USA* **115**, E6191-E6200 (2018).
89. R. Zhang, G. M. Alushin, A. Brown, E. Nogales, Mechanistic Origin of Microtubule Dynamic Instability and Its Modulation by EB Proteins. *Cell* **162**, 849-859 (2015).
90. J. Löwe, H. Li, K. H. Downing, E. Nogales, Refined structure of alpha beta-tubulin at 3.5 A resolution. *J Mol Biol* **313**, 1045-1057 (2001).
91. K. Suhre, Y.-H. Sanejouand, ElNémo: a normal mode web server for protein movement analysis and the generation of templates for molecular replacement. *Nucleic acids research* **32**, W610-W614 (2004).
92. A. R. Atilgan *et al.*, Anisotropy of fluctuation dynamics of proteins with an elastic network model. *Biophys J* **80**, 505-515 (2001).
93. J. A. Maier *et al.*, ff14SB: Improving the Accuracy of Protein Side Chain and Backbone Parameters from ff99SB. *Journal of Chemical Theory and Computation* **11**, 3696-3713 (2015).
94. A. V. Onufriev, D. A. Case, Generalized Born Implicit Solvent Models for Biomolecules. *Annu Rev Biophys* **48**, 275-296 (2019).
95. J. F. Díaz, J. M. Andreu, Assembly of Purified GDP-Tubulin into Microtubules induced by Taxol and Taxotere: Reversibility, Ligand Stoichiometry, and Competition. *Biochemistry* **32**, 2747-2755 (1993).
96. V. Siahaan *et al.*, Kinetically distinct phases of tau on microtubules regulate kinesin motors and severing enzymes. *Nat Cell Biol* **21**, 1086-1092 (2019).
97. M. Castoldi, A. V. Popov, Purification of brain tubulin through two cycles of polymerization-depolymerization in a high-molarity buffer. *Protein Expr Purif* **32**, 83-88 (2003).
98. J. Schindelin *et al.*, Fiji: an open-source platform for biological-image analysis. *Nature Methods* **9**, 676-682 (2012).

1283 ***Supplementary Information.***

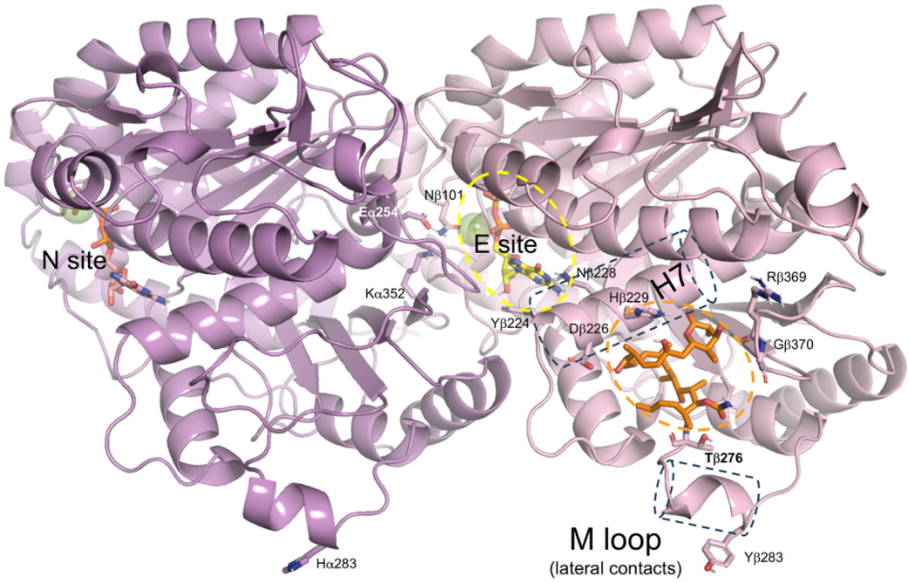

1284

1285 **Figure S1. Helix H7 as a transducer of conformational changes between the taxane-**
1286 **binding site (orange oval), the exchangeable nucleotide site (E site, yellow oval) and the**
1287 **M-loop (an alpha-helix when PFs are associated laterally)**. Ribbon representation of the
1288 interdimer interface from a compressed PF (β1, light pink and α2, dark pink) with bound
1289 discodermolide (C atoms in orange) displayed as a representative taxane site-binding ligand. The
1290 C atoms of the GDP and GTP nucleotides are colored yellow and salmon, respectively. Mg^{2+} ions
1291 are displayed as green spheres and relevant residues mentioned in the text have been labeled.
1292

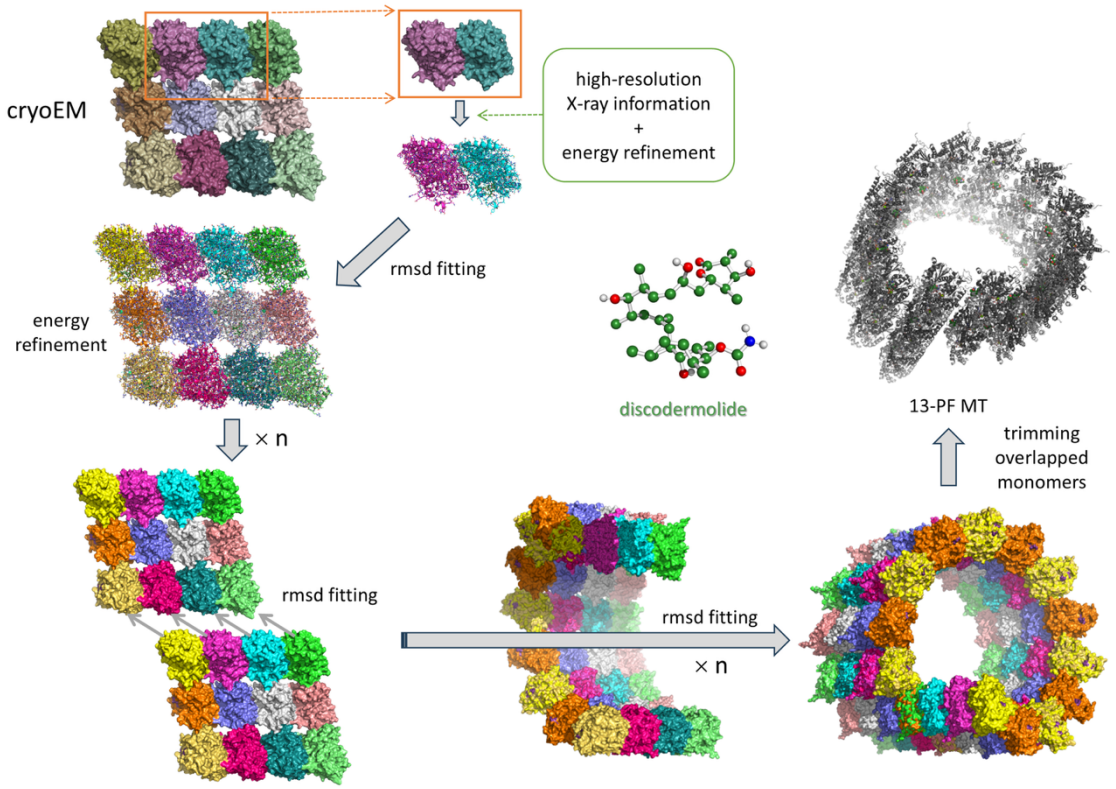

Figure S2. Schematic describing the procedure followed for constructing a full turn of a 13-PF compacted MT fragment with one discodermolide (DDM) molecule bound to the β subunit of each tubulin dimer (https://modelarchive.org/doi/10.5452/ma-ir5i7). Briefly, the initial template was provided by a short MT patch consisting of three laterally associated PFs, each made up of two head-to-tail concatenated tubulin dimers, as deposited in the Protein Data Bank with id. 3JAK. The interdimer interfaces in this cryo-EM structure were optimized with the aid of information provided by the high-resolution X-ray crystal structures 8BDE and 8BDF (for the GDP and GTP nucleotides, Mg^{2+} ions and hydration shell waters) and 5LXT (for the ligand bound at the taxane site in β-tubulin) together with energy refinement using the AMBER force field. The resulting optimized patch was replicated six times in PyMOL. The (α1:β1-α2:β2) stretch of the first copy was then best-fit superimposed onto the (α1":β1"-α2":β2") stretch of the original refined model. Thereafter, the (α1:β1-α2:β2) stretch of each remaining copy was best-fit superimposed onto the (α1":β1"-α2":β2") stretch of the preceding model. This process led quite naturally to formation of a tubular structure consisting of 13 straight PFs with one DDM molecule lodged in the taxane site of every β subunit. Lastly, the macromolecular ensemble was (i) cleaned up by removing the redundant subunit copies used for the superposition and (ii) energy refined in the AMBER force field. A similar procedure was followed to obtain the other complexes reported in this paper, as described in the corresponding entries of the ModelArchive repository. For epothilone B and zampanolide, additional use was made of normal mode analysis to create the 12- and 15-PF MT structures (ModelArchive entries ma-2embb and ma-qcuyh, respectively), as reported previously for paclitaxel (ma-rkctk).

Supp. Movie 1: Representative time-resolved fiber diffraction images. Sequence of images showing fiber diffraction patterns of Apo-MTs and their structural response to the addition of an 2x excess of drug at time = 40 s. (**A** paclitaxel, **B** docetaxel, **C** baccatin III, **D** laulimalide)

Supp. Movie 2: Conformational changes observed by calculating the first non-trivial normal mode for a MT patch consisting of three laterally associated dimers of dimers (PDB id. 6DPV) using the elNemo web server and the default amplitude value. The three views correspond to three orthologous viewpoints. Note that (i) greater amplitudes can be achieved if a bound ligand further stretches the structure along the normal mode and locks the ensemble in this state until ligand

dissociation takes place, and (ii) a decrease in lateral curvature will result in an increase in the number of component PFs and vice versa.

Supp. Movie 3. Representative video of Kif5B-eGFP movement along drug-stabilized MTs. 1-minute video of 10.8 nM Kif5B-eGFP using a 488 nm laser (20% laser intensity, 300 ms exposure) was acquired with no delay (20 fps).

Supp. Movie 4. Tau binding to zampanolide-stabilized MTs. 4 min videos of 5 nM tau-mCherry using a 561 nm laser (30% intensity, 200 ms exposure) were acquired every 7 s.

Supp. Movie 5. Tau binding to discodermolide-stabilized MTs. 4 min videos of 5 nM tau-mCherry using a 561 nm laser (30% intensity, 200 ms exposure) were acquired every 7 s.

Supp. Movie 6. Tau binding to laulimalide-stabilized MTs. 4 min videos of 5 nM tau-mCherry using a 561 nm laser (30% intensity, 200 ms exposure) were acquired every 7 s.

Supp. Movie 7. Tau binding to epothilone B-stabilized MTs. Sequential 4 min videos of (**A**) 10 nM and (**B**) 40 nM tau-mCherry using a 561 nm laser (30% intensity, 200 ms exposure) were acquired every 7 s.

Supp. Movie 8. Tau binding to docetaxel-stabilized MTs. Sequential 4 min videos of (**A**) 10 nM and (**B**) 40 nM tau-mCherry using a 561 nm laser (30% intensity, 200 ms exposure) were acquired every 7 s.

Supp. Movie 9. Tau binding to peloruside A-stabilized MTs. Sequential 4 min videos of (**A**) 5 nM, (**B**)10 nM and (**C**) 40 nM tau-mCherry using a 561 nm laser (30% intensity, 200 ms exposure) were acquired every 7 s.

Supp. Movie 10. tau binding to pelophen B-stabilized MTs. Sequential 4 min videos of (**A**) 10 nM and (**B**) 40 nM tau-mCherry using a 561 nm laser (30% intensity, 200 ms exposure) were acquired every 7 s.

Supp. Movie 11: Conformational changes observed by calculating the first non-trivial normal mode for a short full-circle MT consisting of twelve laterally associated PFs using the elNemo web server and twice the default amplitude value. The three views correspond to three orthologous viewpoints. Note that the motion shown will lead to sealing of the PF gap between the first and the twelfth PF.